



A systematic study of pipe and electrical connections for multi-stack vanadium redox flow battery modules considering electrolyte transport delays

Shaojin Wang^a, Yang Li^{b,*}, Chengyan Li^a, Xifeng Lin^a, Wenbo Ma^c, Nannan Tong^c, Binyu Xiong^{a,d,**}

^a School of Automation, Wuhan University of Technology, Wuhan, China

^b Department of Electrical Engineering, Chalmers University of Technology, Sweden

^c State Information Center, Beijing, China

^d Hubei Province New Energy Power Battery Engineering Research Center, Wuhan, China

ARTICLE INFO

Keywords:

Vanadium redox flow battery
Multi-stack module
Transport delay
Pipe connection
Electrical connection

ABSTRACT

In multi-stack vanadium redox flow battery (VRB) modules, transport delays caused by variations in pipe structure and length can lead to imbalanced electrolyte distribution, higher efficiency losses, and reduced capacity utilization compared to single-stack systems. These limitations pose significant challenges to the scalability of VRBs for grid-scale energy storage. In this paper, we present a systematic study of various multi-stack VRB module configurations using a high-fidelity model that explicitly incorporates transport delays. A total of 208 multi-stack configurations are categorized and analyzed based on two key factors: pipe connections and electrical connections. Pipe connections include T-shape pipe flowing through the stack (T-shaped) and positive and negative tanks on the same side (same-side), cross-shape pipe flowing through the stack (cross-shaped) and positive and negative tanks on the opposite side (opposite-side), T-shaped opposite-side, cross-shaped same-side. Electrical connections include series, parallel, and mixed layouts. Simulation results identify the cross-shaped opposite-side pipe connection as optimal in terms of both capacity utilization and energy efficiency. Among electrical layouts, a 3p2s configuration (three stacks in parallel \times two stacks in series) demonstrates the best system-level performance. The study further explores the impact of different initial states of charge and operating temperatures. In addition, an in-depth techno-economic assessment is performed to evaluate the practical feasibility of all considered configurations. By explicitly integrating transport delay dynamics, the proposed modeling framework enhances the predictive accuracy of VRB system performance. The findings provide quantitative insights for the design and optimization of scalable, high-efficiency multi-stack VRB systems suitable for grid-scale deployment.

1. Introduction

As global climate change accelerates and environmental degradation worsens, the transition to renewable energy as the cornerstone of energy transformation has become increasingly imperative [1,2]. To advance the transition and upgrading of the energy structure while promoting green development in both the economy and society, many countries have set carbon neutrality targets. Large-scale energy storage technologies play a crucial role in ensuring a stable and continuous electricity supply, improving power quality, and supporting the reliable operation

of the power grid [3–6]. Among these technologies, the vanadium redox flow battery (VRB) has gained significant attention due to its unique advantages, including high safety, long cycle life, and environmental friendliness [7–9]. With its promising market potential and extensive practical applications, VRB is expected to see widespread adoption [10–12].

In practical applications, a VRB module consists of multiple single stacks connected in parallel or series, which forms a larger-scale VRB energy storage system (ESS) capable of delivering higher power output and energy storage capacity [13]. Such a system comprises multiple stacks, an electrolyte transport system, and a battery management

* Corresponding author.

** Corresponding author at: School of Automation, Wuhan University of Technology, Wuhan, China.

E-mail addresses: yangli@ieee.org (Y. Li), bxiong2@whut.edu.cn (B. Xiong).

<https://doi.org/10.1016/j.cej.2025.164929>

Received 11 March 2025; Received in revised form 30 May 2025; Accepted 14 June 2025

Available online 17 June 2025

1385-8947/© 2025 Elsevier B.V. All rights reserved, including those for text and data mining, AI training, and similar technologies.

| Nomenclature | | η_Q | capacity utilization |
|---------------------|--|---------------------|--|
| E | terminal voltage | V_σ | degree of inconsistency |
| N_s | number of stacks | σ | standard deviation |
| N_c | number of cells | <i>Subscript</i> | |
| E_0 | Standard electrode potential | stack | single stack |
| R | universal gas constant | ocv | open-circuit voltage |
| F | Faraday's constant | ohm | ohmic |
| T | temperature | act | activation |
| c | ion concentration | con | concentration |
| I | battery current | s | stack |
| i_0 | exchange current density | t | tank |
| R | resistance | 2 | V^{2+} ion |
| A_{ed} | electrode surface area | 3 | V^{3+} ion |
| Q_f | flow rate | 4 | VO^{2+} ion |
| V | pipe volume | 5 | VO_2^+ ion |
| L | pipe length | n | vanadium oxidation state |
| r | pipe radius | d | transport delay |
| U | battery voltage | j | j th stage pipe |
| t | duration | ch | charging |
| SOC_{ch} | charging cut-off SOC | dch | discharging |
| SOC_{dch} | discharging cut-off SOC | max | maximum |
| z | number of electrons transferred in the redox reaction | <i>Superscript</i> | |
| N_{total} | the number of multi-stack module connection | i | i th stack of multi-stack module |
| t_d | transport time for the electrolyte flowing from the tank through the stack | t | tank |
| N_p | the number of pipe connection combinations | <i>Abbreviation</i> | |
| N_e | the number of electrical connection combinations | VRB | vanadium redox flow battery |
| Q | usable capacity of single stack | BMS | battery management system |
| Q^{N_s} | usable capacity of N_s -stack module | ESS | energy storage system |
| G | multi-stack module output parameter | SOC | state of charge |
| g | single-stack output parameter | ECM | equivalent-circuit model |
| \bar{g} | average value of output parameter | CE | coulomb efficiency |
| $LOSS_{power}$ | power loss | VE | voltage efficiency |
| $Cost_{O\&M}$ | operational and maintenance cost | EE | energy efficiency |
| $Cost_{install}$ | installation cost | SE | system efficiency |
| $Cycle_{life}$ | cycle number of the full life of the system | 6 s | six stacks in series |
| p_p | electricity purchase price | 6p | six stacks in parallel |
| y | y th year | 3s2p | three stacks in series \times two stacks in parallel |
| Y | system lifespan | 3p2s | three stacks in parallel \times two stacks in series |
| $N_{cycle}(y)$ | equivalent 100% cycle number of y th year | 2s3p | two stacks in series \times three stacks in parallel |
| $O\&M(y)$ | operation and maintenance cost ratio of the y th year | 2p3s | two stacks in parallel \times three stacks in series |
| C_E | energy installation cost | 2p3s | two stacks in parallel \times three stacks in series |
| C_P | power installation cost | T-shaped | T-shape pipe flowing through the stack |
| d_{dch} | discharge duration | Cross-shaped | cross-shape pipe flowing through the stack |
| <i>Greek symbol</i> | | Same-side | positive and negative tanks on the same side |
| $V_\sigma(I)$ | degree of inconsistency of the current | Opposite-side | positive and negative tanks on the opposite side |
| $V_\sigma(U)$ | degree of inconsistency of the voltage | LCOS | Levelized cost of storage |
| η_{CE} | cycle efficiency of the ESS | DR | discount rate |
| η | overpotential | | |

system (BMS). The number of stacks directly determines the overall power output, while the electrolyte transport system ensures proper electrolyte circulation. The BMS is responsible for monitoring, controlling, and maintaining the battery performance [14]. A key advantage of the multi-stack system is its modular design, which enhances both flexibility and scalability. Each stack functions as an independent module, facilitating individual design and manufacturing. By varying electrical and piping configurations, large-scale ESSs can be adapted to different application requirements. This modular design not only simplifies maintenance but also significantly enhances system scalability.

In a multi-stack VRB module, major challenges such as shunt

currents and pump losses often lead to reduced system efficiency (SE) [15,16]. To address this problem, Qiang et al. [17] compare representative pipeline system designs and improve the balance between SE and compactness through intrinsic design. They suggest designing longer and wider pipes to minimize shunt currents with acceptable flow resistance, which facilitates efficiency but is limited in terms of compactness. Wandschneider et al. [18] modelled shunt current of VRB. The impact of shunt currents on the coulombic efficiency (CE) and energy efficiency (EE) of the system is investigated. They showed that longer pipes are a common solution to the external shunt currents. On this basis, Zhao et al. [19] analyzed the shunt currents based on different electrical

connections. They found that the parallel-connected stack modules achieved the highest CE and EE, as these configurations eliminated shunt current losses in the pipe system.

In addition, the arrangement and connection methods of the multiple stacks need critical considerations in the design and assembly of multi-stack ESSs. The varying internal resistance of each stack leads to differences in ohmic polarization, activation, and concentration overpotentials, resulting in voltage inconsistency among stacks. According to the theory of constraints, such inconsistency within the module can impose performance limitations on VRB operation. In other battery systems, the inconsistency problem has been widely investigated [20–24]. However, in VRBs, relevant research is rare and underdeveloped. Inconsistency among stacks can lead to premature charge-discharge cutoffs during cycling, preventing the system from achieving its intended capacity and efficiency. Over time, this degrades the multi-stack performance in long-term operation and accelerates the reduction of VRB lifespan [25]. In a pioneer work, Chen et al. [26] investigated the correlation between stack layout and performance by adjusting stack arrangements. They proposed 35 different configurations for an 8-stack 250-kW module and demonstrated that grouping stacks with similar resistances in the same branch significantly enhances the module's charge capacity and overall charging capability. Apart from the stack arrangement, pipe connection is another critical factor influencing system performance. However, conventional research has largely overlooked this aspect, and systematic, comprehensive studies on multi-stack connections in VRBs are lacking.

To optimize the pipe and electrical connections of multi-stack VRB modules and enhance their performance, this study develops a multi-stack VRB system model that incorporates electrolyte transport delay. For a module consisting of six 32-kW stacks, two types of connections are analyzed: pipe connection and electrical connection. Pipe connections are further categorized based on pipe design and feeding mode, with four pipe types investigated: T-shape pipe flowing through the stack (T-shaped) and positive and negative tanks on the same side (same-side), cross-shape pipe flowing through the stack (cross-shaped) and positive and negative tanks on the opposite side (opposite-side), T-shaped opposite-side, cross-shaped same-side. Electrical connections are classified based on circuit topology and stack layouts, including series, parallel, and mixed connections, resulting in 52 distinct connection types. Mixed connections can be further divided into 50 variations based on different stack layouts. To evaluate the performance of each type of connection, EE and capacity utilization are introduced as the key metrics. Simulations are conducted to assess the impact of various connection configurations on module performance, and the results are used to identify the optimal pipe and the optimal electrical connections. The findings establish a foundational framework for the safe, efficient, and stable implementation of multi-stack VRB modules in large-scale ESSs.

The rest of this paper is organized as follows. Section 2 introduces the multi-stack VRB module model incorporating transport delay. Section 3 describes two typical multi-stack VRB module connections, including pipe and electrical connections. Section 4 presents the simulation results and corresponding evaluation metrics for all multi-stack connections. Finally, Section 5 summarizes the conclusions.

2. Model development

The mathematical model development is based on the conservation of mass and charge, and the assumptions below are made to simplify the model without loss of generality:

- 1) The stack and the tank exhibit continuity in time and space;
- 2) Gas evolution and side reactions are neglected;
- 3) Proton exchange membranes are ideally selective [27];
- 4) The concentration of vanadium ions in the tank and stack is uniform and consistent;
- 5) Resistance remains constant during the cycling.

2.1. Equivalent-circuit model of multi-stack VRB modules

As an example, we present the modeling procedure using the equivalent circuit of a multi-stack VRB module connected in series, as depicted in Fig. 1. The terminal voltage U of the multi-stack module is the sum of the terminal voltages of all stacks, i.e.,

$$U = \sum_{i=1}^{N_s} E_{\text{stack}}^i \quad (1)$$

where E_{stack}^i represents the terminal voltage of the i th stack, N_s is the number of stacks. E_{stack}^i is calculated as [28].

$$E_{\text{stack}}^i = E_{\text{ocv}}^i + \eta_{\text{ohm}}^i + \eta_{\text{act}}^i + \eta_{\text{con}}^i \quad (2)$$

where η is overpotential. The subscripts “ocv”, “ohm”, “act”, and “con” denote open-circuit voltage, ohmic, activation, and concentration, respectively.

Based on the Nernst equation, the open-circuit voltage E_{ocv}^i is calculated by

$$E_{\text{ocv}}^i = E_0^i + \frac{RT^i}{zF} \ln \left(\frac{c_2^i c_5^i}{c_3^i c_4^i} \right) \quad (3)$$

where R is the universal gas constant, z is the number of electrons transferred in the redox reaction, and F is the Faraday's constant. E_0^i , T^i , and c^i are the standard electrode potential, temperature, and ion concentration of the i th stack, respectively. The subscripts 2, 3, 4, and 5 represent species V^{2+} , V^{3+} , VO^{2+} , and VO_2^+ , respectively.

The ohmic overpotential η_{ohm}^i of the i th stack is calculated by

$$\eta_{\text{ohm}}^i = I^i R_{\text{ohm}}^i \quad (4)$$

where I^i is the battery current (positive for charging and negative for discharging) of the i th stack, and R_{ohm}^i is the contact resistance between the electrolyte and the internal components of the i th stack.

The activation overpotential η_{act}^i of the i th stack is calculated as:

$$\eta_{\text{act}}^i = N_c^i \frac{RT^i}{zF} \ln \left(\frac{i_0^i}{I^i / A_{\text{ed}}^i} \right) \quad (5)$$

where N_c^i , i_0^i , and A_{ed}^i are the number of cells, the exchange current density on the electrode surface, and the electrode surface area of the i th stack, respectively.

The concentration overpotential η_{con}^i of the i th stack is calculated as:

$$\eta_{\text{con}}^i = \frac{RT^i}{zF} \ln \left(1 - \frac{I^i}{1.6 \times 10^{-4} \times z F Q_f^i c^t} \right) \quad (6)$$

where c^t is the concentration of the tank, Q_f^i is the flow rate of the i th stack, and Q_f is the flow rate of the module.

Without considering the side reactions, the concentration of vanadium ions in the stack and tank of the multi-stack module is calculated as follows based on mass conservation [29,30]:

$$\begin{cases} V_s \frac{dc_n^i}{dt} = Q_f^i (c_n^t - c_n^i) + \frac{N_c^i I^i}{zF} \\ V_t \frac{dc_n^t}{dt} = N_s Q_f \left(\frac{1}{N_s} \sum_{i=1}^{N_s} c_n^i - c_n^t \right) \end{cases} \quad (7)$$

where the superscript t represents the tank, and the subscript n represents the vanadium oxidation state in the stack.

Since the focus of the present study is on pipe and electrical connections, the following assumptions are made to simplify the analysis. First, all stacks share an identical design with $E_0^i = E_0$, $N_c^i = N_c$, and $A_{\text{ed}}^i = A_{\text{ed}}$. Second, the temperature is uniformly controlled, which gives

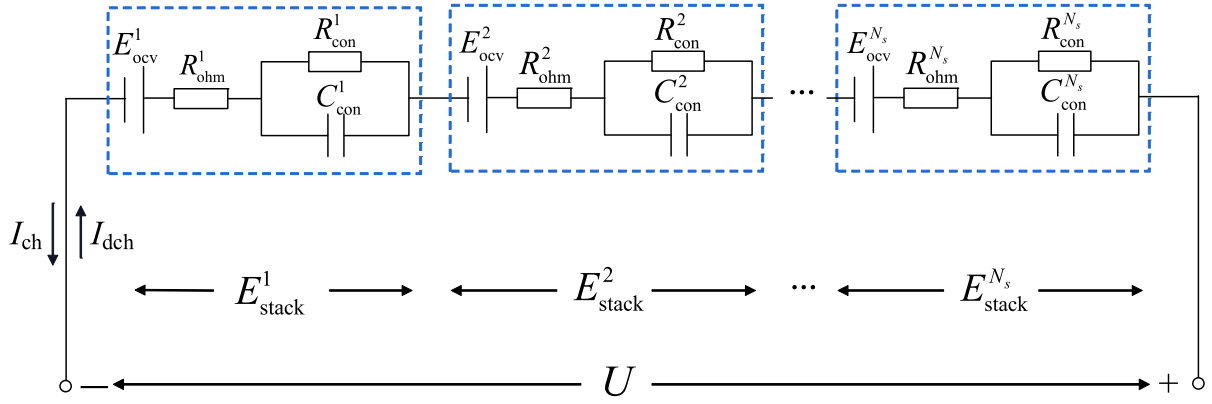


Fig. 1. Equivalent-circuit model of a multi-stack VRB module connected in series.

$T^i = T$. Third, the flow distribution is uniform, which leads to $Q_f^i = Q_f$. Finally, for the series-connected module, all stack currents equal the module current, i.e., $I^i = I$.

2.2. Multi-stack VRB module model incorporating transport delay

The multi-stack series module, as illustrated in Fig. 2, connects the tank to the circulatory system of each stack's pipes. It typically comprises multi-stage pipes, where each stage is designed with different diameters and other factors that influence the pipe structure and length. This design ensures that the electrolyte meets specific performance requirements as it flows through each stack. The transport delay time from the tank to the stack is not simply a single delay but rather the cumulative delay resulting from the electrolyte's passage through each stage of the pipe system.

The transport delay time for the multi-stack VRB module is calculated as [25]

$$t_d^i = \sum_{j=1}^m t_{d,j}^i = \sum_{j=1}^m \frac{V_j^i}{Q_{f,j}^i} = \sum_{j=1}^m \frac{L_{p,j}^i \pi (r_{p,j}^i)^2}{Q_{f,j}^i} \quad (8)$$

where m is the number of stages of the pipe, which is assumed to be the same for all stacks, t_d^i is the transport time for the electrolyte flowing from the tank through the i th stack, and $t_{d,j}^i$, V_j^i , $Q_{f,j}^i$, $L_{p,j}^i$, and $r_{p,j}^i$ represent the transport delay time, pipe volume, pipe flow rate, pipe length, and radius of the electrolyte flowing from the tank through the j th stage pipe of the i th stack, respectively.

Combining (7) and (8), and considering the assumptions made in the previous section, a multi-stack VRB module model incorporating transport delay is derived as

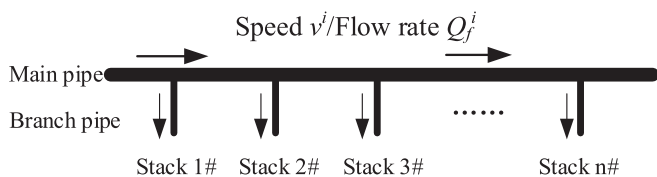


Fig. 2. Schematic diagram of electrolyte transport in a multi-stack VRB module.

$$\begin{cases} V_s \frac{dc_n^i}{dt} = Q_f \left(c_n^i \left(t - \sum_{j=1}^m \frac{L_{p,j}^i \pi (r_{p,j}^i)^2}{Q_{f,j}^i} \right) - c_n^i \right) + \frac{N_s I}{zF} \\ V_r \frac{dc_n^t}{dt} = N_s Q_f \left(\frac{1}{N_s} \sum_{i=1}^{N_s} c_n^i \left(t - \sum_{j=1}^m \frac{L_{p,j}^i \pi (r_{p,j}^i)^2}{Q_{f,j}^i} \right) - c_n^t \right) \end{cases} \quad (9)$$

$$\text{when } t < t_d^i, c_n^t \left(t - \sum_{j=1}^m \frac{L_{p,j}^i \pi (r_{p,j}^i)^2}{Q_{f,j}^i} \right) = c_n^t(0), c_n^{s,i} \left(t - \sum_{j=1}^m \frac{L_{p,j}^i \pi (r_{p,j}^i)^2}{Q_{f,j}^i} \right) = c_n^{s,i}(0).$$

This model can be modified for other multi-stack configurations discussed next in Section 3, though detailed models are omitted in the present work for brevity.

The transport delays of multi-stack modules present significant challenges for grid-scale applications, particularly in terms of response speed and system coordination. Unlike single-stack systems, multi-stack configurations require the electrolyte to flow through extended pipes and multiple stacks, resulting in longer flow paths. These transport delays introduce response lags that cause uneven voltage and current distribution across stacks. In addition, the increased fluidic and electrical complexity complicates system design and maintenance, further limiting scalability and operating costs.

3. Pipe and electrical connections

3.1. Pipe connection types

In this study, a VRB module consisting of six 32-kW stacks is analyzed as a case study. The pipe connection topology is categorized considering shape design and feeding mode, i.e., the way the electrolyte flows to the stacks and the tank placement. Shape design is classified into T-shaped and cross-shaped, while feeding mode is divided into same-side and opposite-side. As shown in Fig. 3, the four typical pipe connection types are T-shaped same-side, T-shaped opposite-side, cross-shaped same-side, and cross-shaped opposite-side.

In the T-shaped connection, pipes are arranged sequentially according to stack order, with the flow progressing from the nearest to the farthest stack. The main pipe connects to the branch pipes at regular intervals, which allows the electrolyte to flow through the main pipe, enter each stack via its branch pipe, and exit in a similar manner. In contrast, the cross-shaped connection topology features a cross-configured pipe layout. As the electrolyte flows through the main pipe toward the stacks, it simultaneously splits into two branches, each directing the electrolyte to a separate stack. The T-shaped connection topology is well-suited for applications where the stack layout is more

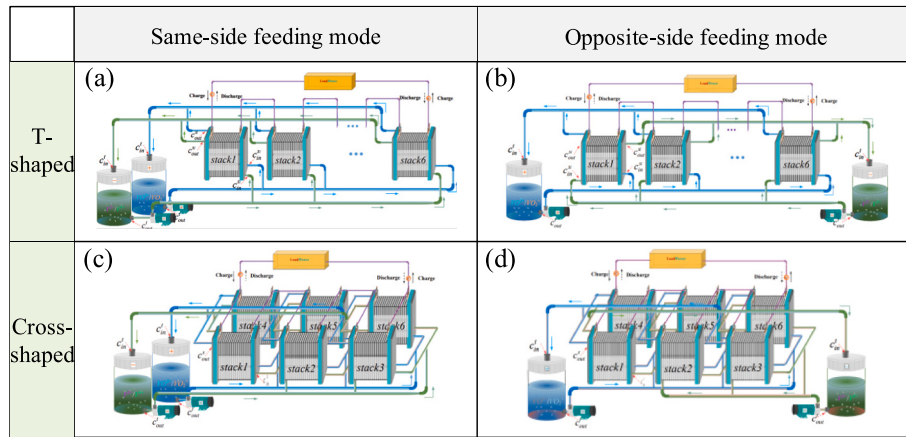


Fig. 3. Four typical pipe connection types for a module consisting of six 32-kW stacks. (a) T-shaped same-side; (b) T-shaped opposite-side; (c) Cross-shaped same-side; (d) Cross-shaped opposite-side.

spread out, as it effectively reduces the resistance and ensures a smooth electrolyte flow. In contrast, the cross-shaped connection is more compact and provides more uniform electrolyte distribution across all stacks. This pipe connection also ensures that each stack receives a sufficient electrolyte supply while enhancing space utilization and reducing the system footprint.

The opposite-side mode can employ the concentration distribution in the pipe to balance the total potentials from both the positive and negative sides, which effectively reduces the difference in stack voltages during the whole charging-discharging operation. Therefore opposite-side mode can effectively reduce the problem of premature cut-off.

3.2. Electrical connection types

3.2.1. Electrical connections with different circuit topology

There are three main circuit topologies: series connection (six stacks in series, 6s), parallel connection (six stacks in parallel, 6p), and mixed connection. The mixed connection can be further divided into two categories of configurations: series-parallel and parallel-series. In the series-parallel configuration, stacks are first connected in series and then in parallel, with two common configurations: three stacks in series \times two stacks in parallel (3s2p) and two stacks in series \times three stacks in parallel (2s3p). In contrast, the parallel-series configuration first group stacks in parallel before connecting them in series, resulting in two configurations: two stacks in parallel \times three stacks in series (2p3s) and three stacks in parallel \times two stacks in series (3p2s).

In a series connection, the voltages of the individual stacks are summed, increasing the module voltage, and all stacks share the same current. Series connections are preferred for high-voltage applications but sensitive to single-stack failures, which can affect overall system performance. In a parallel connection, the current is distributed among the stacks, increasing the module current while maintaining a common voltage in the stacks. This setup enhances output current and power, making it suitable for high-current or large-capacity applications. Unlike series connections, a single-stack failure does not impact the performance of other stacks. A mixed connection allows for flexible adjustment of module voltage and current to meet specific requirements. However, compared to pure series and parallel connections, mixed connections introduce greater design complexity and require precise control and management to avoid issues such as voltage or current inconsistency. Fig. 4 illustrates the typical circuit connections for the six-stack module.

3.2.2. Electrical connections based on stack layout

This section presents different stack layouts, i.e., how stacks are arranged in the multi-stack module. Only mixed connections are examined

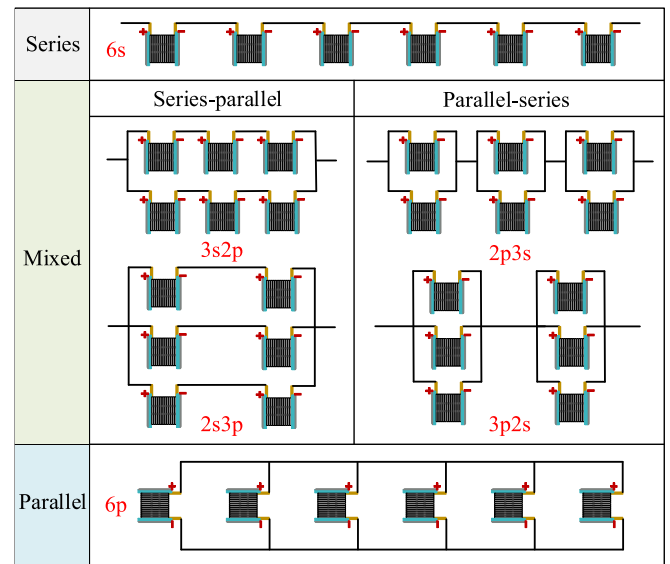


Fig. 4. Typical circuit connections for a six-stack VRB module.

since the stack layout does not influence series and parallel connections. The following tables provide detailed layouts of six stacks: Tables 1 and 2 show the 3s2p and 2s3p series-parallel layouts, while Tables 3 and 4 present the 3p2s and 2p3s layouts.

For the multi-stack module configured as 3s2p and 3p2s, only one branch needs to be determined to finalize the layout. As a result, there are $C_6^3/2 = 10$ distinct layouts for both configurations. In contrast, for 2s3p and 2p3s, two branches need to be determined to complete the layout. Consequently, there are $C_6^4 = 15$ distinct layouts for these two configurations.

3.3. Analysis of multi-stack module connections

The total number of distinct connection methods, N_{total} , that can be developed for a multi-stack module consisting of six 32-kW stacks, is calculated by

$$N_{\text{total}} = N_p \times N_e = (2 \times 2) \times [2 + (10 + 15) \times 2] = 208 \quad (10)$$

where N_p and N_e are the number of pipe connection combinations and the number of electrical connection combinations, respectively.

Table 1
All 10 layouts of the 3s2p series-parallel configuration.

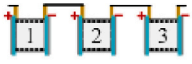

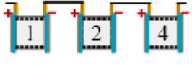
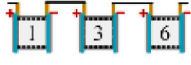

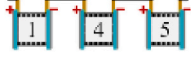



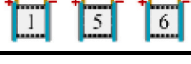
| Case | Branch 1 | Case | Branch 1 |
|------|---|------|--|
| 1 |  | 6 |  |
| 2 |  | 7 |  |
| 3 |  | 8 |  |
| 4 |  | 9 |  |
| 5 |  | 10 |  |

Table 2
All 15 layouts of the 2s3p series-parallel configuration.

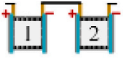
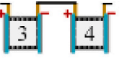
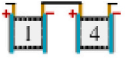
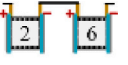

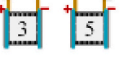






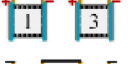
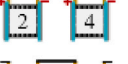
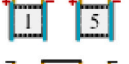
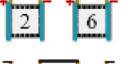
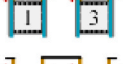

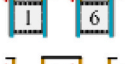







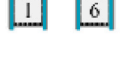
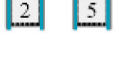


| Case | Branch 1 | Branch 2 | Case | Branch 1 | Branch 2 |
|------|---|---|------|--|---|
| 1 |  |  | 9 |  |  |
| 2 |  |  | 10 |  |  |
| 3 |  |  | 11 |  |  |
| 4 |  |  | 12 |  |  |
| 5 |  |  | 13 |  |  |
| 6 |  |  | 14 |  |  |
| 7 |  |  | 15 |  |  |
| 8 |  |  | | | |

Fig. 5 presents a comprehensive overview of all possible connections for the multi-stack module based on the preceding analysis. The detailed examination of connection methods provides valuable insights for the design and optimization of the multi-stack VRB module performance.

4. Results and discussion

4.1. Parameter settings

In this section, charging and discharging simulations are conducted using MATLAB to evaluate the performance of a multi-stack VRB module with 208 pipe and electrical connection configurations. The charging and discharging processes are simulated by replicating the conditions of the relevant experimental environment, where the ambient temperature is maintained at 25 °C. The electrolyte volume is set at 4 m³, with a total vanadium ion concentration of 2 mol·L⁻¹. The pump flow rate is configured at 5.6 L·s⁻¹, and the initial state of charge (SOC) is set to 20%. The charging and discharging cut-off voltages are 1.671 V and

1.329 V, respectively, both for a single cell. The total length of the main pipe is 15 m, the radius of the main pipe is 0.15 m, the length of the branch pipe is 0.5 m, and the radius of the branch pipe is 0.02 m. Furthermore, each stack features a constant resistivity of 2 Ω·cm², an equilibrium potential of 1.4 V, 60 cells per stack, and an electrode area of 0.45 m². The current density settings for charging and discharging vary based on the configuration: 1000 A·m⁻² for 6 s, 3 × 1000 A·m⁻² for 3s2p and 2p3s, 2 × 1000 A·m⁻² for 2s3p and 3p2s, and 6 × 1000 A·m⁻² for the 6p.

4.2. Performance evaluation metrics

The performance of an ESS is typically assessed based on its efficiency, defined as the ratio of input and output energy. Efficiency not only reflects the energy losses during conversion but also serves as a critical indicator of overall system performance. Key performance metrics include coulombic efficiency (CE), voltage efficiency (VE), energy efficiency (EE), and capacity utilization (η_Q).

Table 3
All 10 layouts of the 3p2s parallel-series configuration.

| Case | Branch 1 | Case | Branch 1 |
|------|----------|------|----------|
| 1 | | 6 | |
| 2 | | 7 | |
| 3 | | 8 | |
| 4 | | 9 | |
| 5 | | 10 | |

Table 4
All 15 layouts of the 2p3s parallel-series configuration.

| Case | Branch 1 | Branch 2 | Case | Branch 1 | Branch 2 |
|------|----------|----------|------|----------|----------|
| 1 | | | 9 | | |
| 2 | | | 10 | | |
| 3 | | | 11 | | |
| 4 | | | 12 | | |
| 5 | | | 13 | | |
| 6 | | | 14 | | |
| 7 | | | 15 | | |
| 8 | | | | | |

CE is defined as the ratio of the actual power stored or released to the theoretical power stored or released by the battery during charging and discharging. VE refers to the extent of voltage reduction within the cell caused by factors such as ohmic losses and concentration polarization. EE of a system is defined as the ratio of useful work produced to the energy input, which can directly reflect the operational efficiency of the system. Since CE and VE can only indirectly reflect part of the efficiency and have limitations, we use EE as a metric for efficiency in the rest of the work. The mathematical expressions for these efficiencies are as follows [31]:

$$CE = \frac{\int_0^{t_{dch}} I_{dch} dt}{\int_0^{t_{ch}} I_{ch} dt} \times 100\% \quad (11)$$

$$VE = \frac{\int_0^{t_{dch}} U_{dch} dt}{\int_0^{t_{ch}} U_{ch} dt} \quad (12)$$

$$EE = CE \times VE = \frac{\int_0^{t_{dch}} U_{dch} I_{dch} dt}{\int_0^{t_{ch}} U_{ch} I_{ch} dt} \quad (13)$$

where $U_{ch} = U$ and $I_{ch} = I$ represent the terminal voltage and current magnitude of the VRB module during charging, respectively, $U_{dch} = U$ and $I_{dch} = -I$ denote the terminal voltage and the current magnitude during discharging, respectively, and t_{ch} and t_{dch} are the durations of the charging and discharging processes, respectively.

Capacity utilization, denoted by η_Q , is a measure of the battery's effective use of its nominal capacity in practical applications. It is defined as follows [25]:

$$\eta_Q = \frac{Q_{max}^{N_s}}{N_s Q_{max}} \quad (14)$$

where Q and Q^{N_s} represent the usable capacities of a single stack and an N_s -stack module, respectively, and their maximum values, Q_{max} and $Q_{max}^{N_s}$, are calculated by

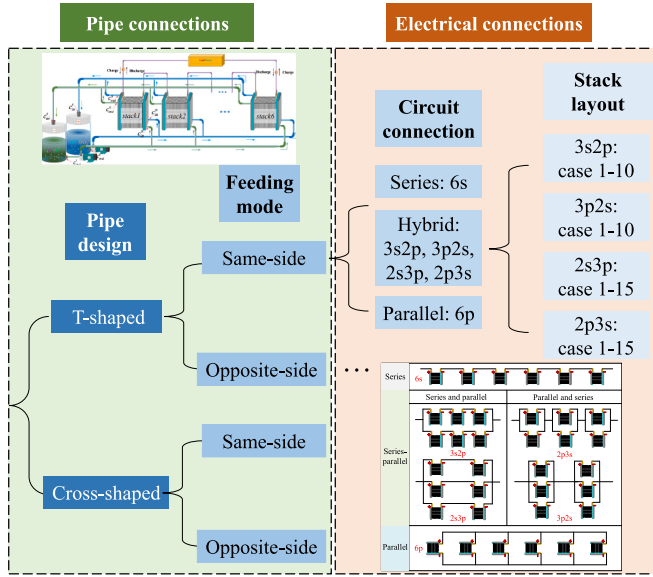


Fig. 5. Classification of multi-stack VRB module connection types based on pipe and electrical connections.

$$Q_{\max} = Q_{\text{ch},\max} + Q_{\text{dch},\max}$$

$$= Q \times \max(\text{SOC}_{\text{ch}}(1), \text{SOC}_{\text{ch}}(2), \dots, \text{SOC}_{\text{ch}}(N_s)) + Q \times [1 - \min(\text{SOC}_{\text{dch}}(1), \text{SOC}_{\text{dch}}(2), \dots, \text{SOC}_{\text{dch}}(N_s))] \quad (15)$$

$$Q_{\max}^{N_s} = Q_{\text{ch},\max}^{N_s} + Q_{\text{dch},\max}^{N_s}$$

$$= Q \times \sum_{i=1}^{N_s} \text{SOC}_{\text{ch}}(i) + Q \times \sum_{i=1}^{N_s} \text{SOC}_{\text{dch}}(i) \quad (16)$$

where subscripts “ch,max” and “dch,max” represent the maximum values during charging and discharging, respectively, $\text{SOC}_{\text{ch}}(i)$ is the charging cut-off SOC of the i th stack, and $\text{SOC}_{\text{dch}}(i)$ is the discharging cut-off SOC of the i th stack.

To quantify the differences in the output parameters across each stack in the multi-stack VRB module, a degree of inconsistency, denoted as V_σ , is introduced to compare the variation of the data. Let the output parameters of the multi-stack module be represented as $G = g(i)$, where $i = 1, 2, \dots, N_s$, and $g(i)$ represents the output parameter of a single stack. We define a metric for the degree of inconsistency, V_σ , as follows [20]:

$$V_\sigma = \frac{\sigma}{\bar{g}} \quad (17)$$

where \bar{g} is the average of the output parameter g , and σ is the standard deviation of the parameter G , calculated by

$$\sigma = \sqrt{\frac{\sum_{i=1}^{N_s} [(g(i) - \bar{g})]^2}{N_s - 1}} \quad (18)$$

The above parameters are used to evaluate the performance of multi-stack VRB modules from multiple perspectives, including charging and discharging efficiency, capacity utilization, and inter-stack inconsistency. This comprehensive analysis enables a more accurate and quantitative assessment of the impact of transport delay on system behavior.

4.3. Results for series and parallel connections

As an example, Fig. 6 presents the simulation results of the multi-stack VRB module in the 6 s and 6p configurations for the T-shaped same-side connection. When the stacks are connected in series, each stack carries the same current, resulting in zero current inconsistency. However, the voltage across each stack differs, so only the variation in

voltage inconsistency is shown, as illustrated in Fig. 6(e). Similarly, when the stacks are connected in parallel, only the variation in current inconsistency is displayed, as shown in Fig. 6(f).

A multi-stack VRB module experiences different charging and discharging durations when connected in series or parallel, which leads to variations in system performance. To better illustrate this difference, the relationship between the degree of inconsistency and the performance of the multi-stack module is investigated. Cycle experiments under series and parallel connections, with three additional pipe connections, are simulated, as shown in Fig. 7. In this double-axis plot, the bars represent the magnitudes of CE, VE, EE, and η_Q on the left y-axis. The line graph on the right y-axis illustrates $V_\sigma(I)$ and $V_\sigma(U)$, which measure current and voltage inconsistency, respectively. The right y-axis is inverted, where higher values indicate better consistency and lower values indicate greater inconsistency.

Table 5 summarizes the optimal connections for various evaluation metrics. Case I refers to the scenario where the pipe design and feeding mode settings are fixed, but the circuit connection is variable. Case II refers to the scenario where the pipe design and circuit connection settings are fixed, but the feeding mode is variable. Case III refers to the scenario where the feeding mode and circuit connection settings are fixed, but the pipe design is variable. In Case I, there is little difference in EE between series and parallel configurations, but η_Q and V_σ perform better in parallel than in series. In Case II, EE and η_Q are higher on the opposite side compared to the same side, with no clear trend in V_σ . In Case III, the cross-shaped connection outperforms the T-shape connection in terms of V_σ , EE, and η_Q .

Case III demonstrates how the compact design of the cross-shaped connection effectively minimizes the effects of transport delay, thereby improving the module's performance. Case II highlights the superiority of the opposite side connection, as it allows the electrolyte to enter the stack from two opposing directions, a key advantage in reducing voltage inconsistency. As shown in Fig. 7, it is evident that feeding mode has a greater impact on the multi-stack module than pipe design. Combined with Table 5, the cross-shaped opposite side configuration exhibits the highest EE, η_Q , and the lowest V_σ among all connections. This demonstrates the advantages of the cross-shaped opposite-side configuration in enhancing the performance of the multi-stack VRB module.

4.4. Results for mixed connections

The simulation results for electrical mixed connections are presented in this section. As an example, Fig. 8 illustrates the simulation results for Case 1 using the T-shaped same-side connection for the 3s2p configuration. As shown in Fig. 8(a), the voltage curves of each stack under the mixed connection exhibit a distinct pattern compared to the voltage ranking in a purely series configuration, which indicates that the mixed connection affects the performance of individual stacks. To further analyze the impact of different mixed connections and layouts on the multi-stack VRB module, we evaluate 50 electrical connection configurations under four pipe connection types. Additional details are provided in Figs. 9 to 12.

Fig. 9 illustrates the multi-stack evaluation metrics for T-shaped same-side under 3s2p, 3p2s, 2s3p and 2p3s. The bars represent efficiency and capacity and correspond to the left y-axis. The line represents the current and voltage inconsistency, corresponding to the right y-axis. 3s2p performs best on average for inconsistency. Case 5 of 3s2p has the best overall performance. Case 1 of 3p2s has the worst overall performance. In Fig. 10, Case 1 of 3s2p has the best overall performance. Case 1 of 3p2s has the worst overall performance. In Fig. 11, Case 7 of 2s3p has the best overall performance. Case 1 of 3s2p has the worst overall performance. In Fig. 12, Case 1 of 3p2s has the best overall performance for all the configurations. Case 1 of 3s2p has the worst overall performance.

To visualize multiple evaluation metrics, the overall performance

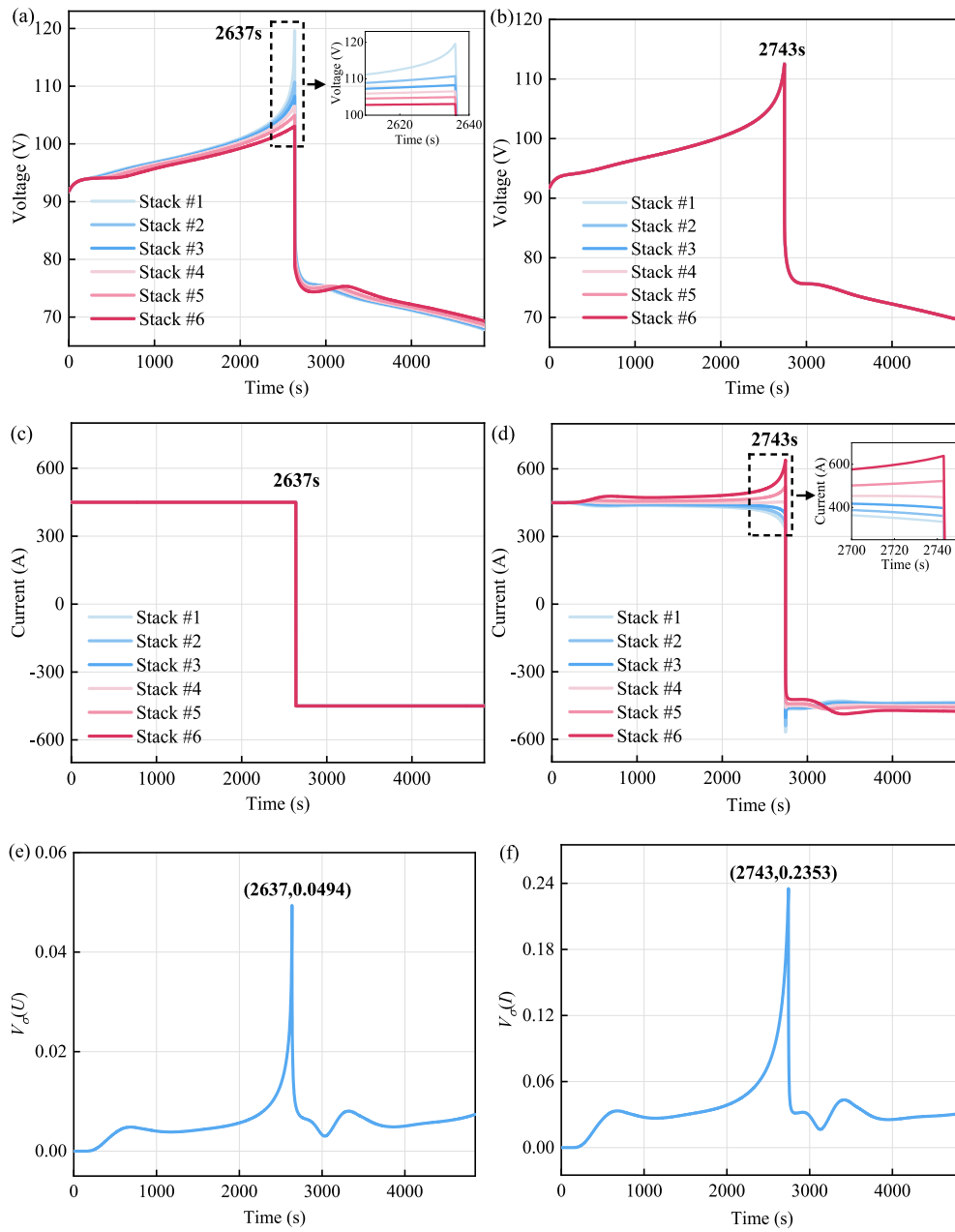


Fig. 6. Simulation results of multi-stack VRB module for different connection configurations: (a) Stack voltages under 6s; (b) Stack voltages under 6p; (c) Stack currents under 6s; (d) Stack currents under 6p; (e) Voltage inconsistency $V_{\sigma}(U)$ under 6s; (f) Current inconsistency $V_{\sigma}(I)$ under 6p.

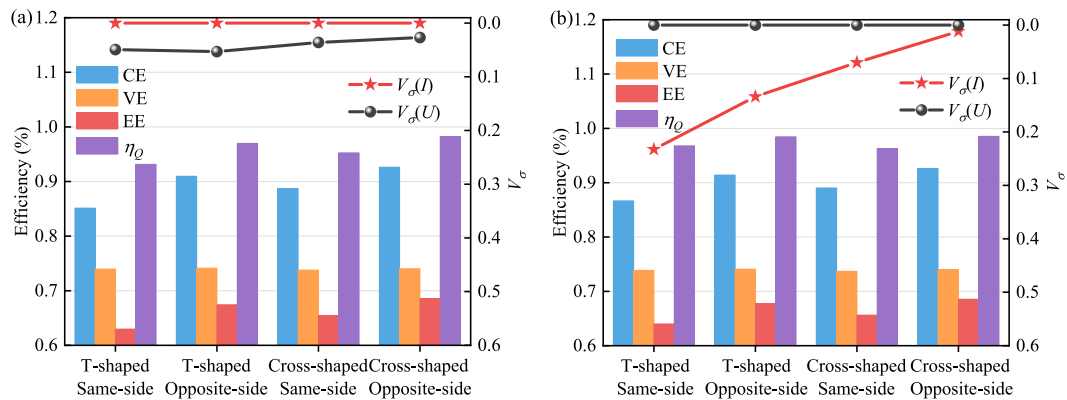


Fig. 7. Performance comparison of the multi-stack VRB module under different electrical connections: (a) Series; (b) Parallel.

Table 5

Optimal connection of multi-stack VRB module under different evaluation metrics.

| Case | Fixed | Variable | Preferred | | |
|----------|----------------------------------|--------------------|-----------------|---------------|---------------------------|
| | | | EE | η_Q | $V_\sigma(I)/V_\sigma(U)$ |
| Case I | Pipe design; feeding mode | Circuit connection | Series/parallel | Series | Series |
| Case II | Pipe design; circuit connection | Feeding mode | Opposite side | Opposite side | – |
| Case III | Feeding mode; circuit connection | Pipe design | Cross-shaped | Cross-shaped | Cross-shaped |

score (OPS) is introduced to comprehensively assess the overall performance of the multi-stack module under different connections. A larger OPS indicates the better overall performance of the multi-stack VRB module. Conversely, a smaller OPS indicates worse performance.

$$\text{OPS} = \text{EE} + \eta_Q - V_\sigma(I) - V_\sigma(U) \quad (19)$$

As shown in Table 6, the optimal electrical stack layout and its OPS value are influenced by the type of circuit connection used in the mixed connection. The table presents the optimal stack layouts and their OPSs for the four electrical mixed connections. The 2p3s configuration achieves the highest average OPS of 1.5633 across all pipe connections,

indicating the best overall performance for the multi-stack module with this connection type. In contrast, the 3p2s configuration shows the lowest average OPS, reflecting the poorest performance. In addition, the results demonstrate that the cross-shaped pile connection outperforms the T-shaped connection, and the opposite-side layout is more effective than the same-side design, which aligns with the findings in Section 3.2. Under the cross-shaped opposite-side configuration, Cases 1, 2, 4, 6, 8, and 10 in the 3p2s configuration achieve the highest OPS of 1.6592. This shows that this multi-stack layout configuration offers optimal performance under mixed connections.

4.5. Performance analysis under different connection configurations

This section analyzes and compares the performance of all 208 connection configurations. The performance metrics for the four pipe connection types, i.e., T-shaped same-side, cross-shaped same-side, T-shaped opposite-side, and cross-shaped opposite-side, are presented in Tables 7–10, respectively. Note that the results for the 3s2p, 2s3p, 3p2s, and 2p3s configurations are reported as the average values across their respective multiple cases.

Tables 7–10 compare the performance of all connection configurations. Among them, the series configuration (6s) exhibits the highest $V_\sigma(U)$ value in all electrical connection methods, which indicates the greatest voltage inconsistency and the lowest reliability since a failure in any single stack can cause an overall system shutdown. In contrast, the parallel configuration (6p) avoids this single-point failure issue but

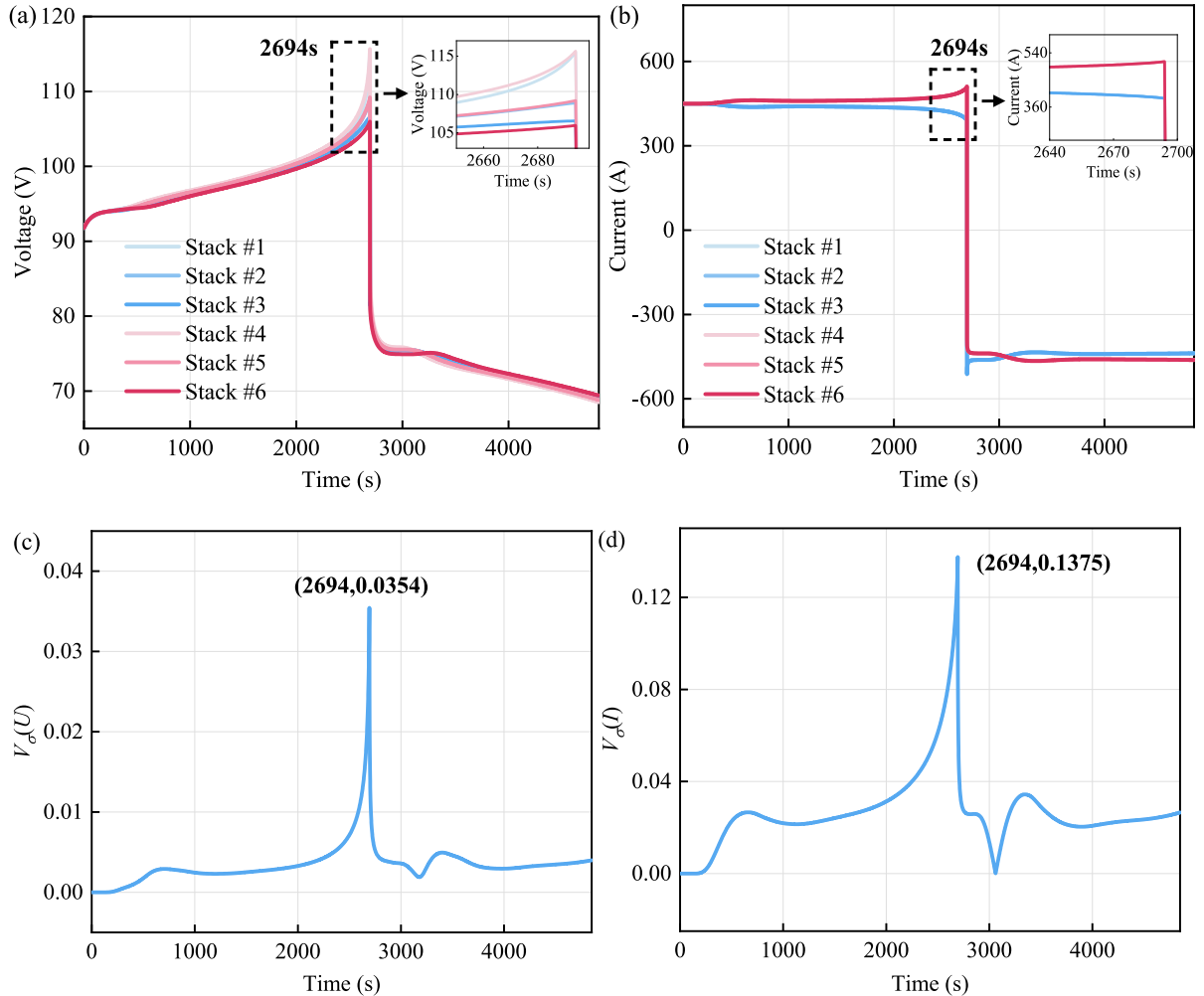


Fig. 8. Multi-stack VRB module simulation results under 3s2p: (a) Voltage of each stack; (b) Current of each stack; (c) Voltage inconsistency $V_\sigma(U)$; (d) Current inconsistency $V_\sigma(I)$.

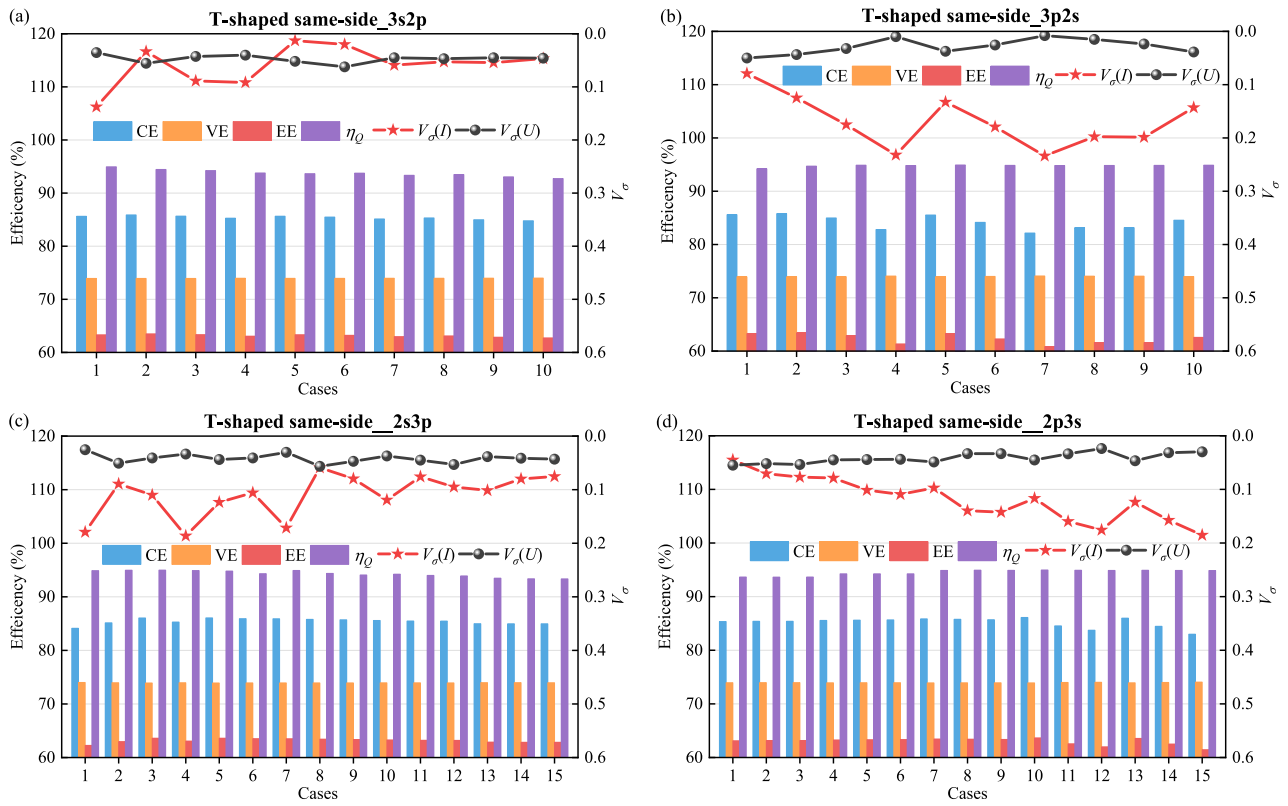


Fig. 9. Performance metrics of multi-stack VRB module under T-shaped same-side in different electrical mixed connections: (a) 3s2p; (b) 3p2s; (c) 2s3p; (d) 2p3s.

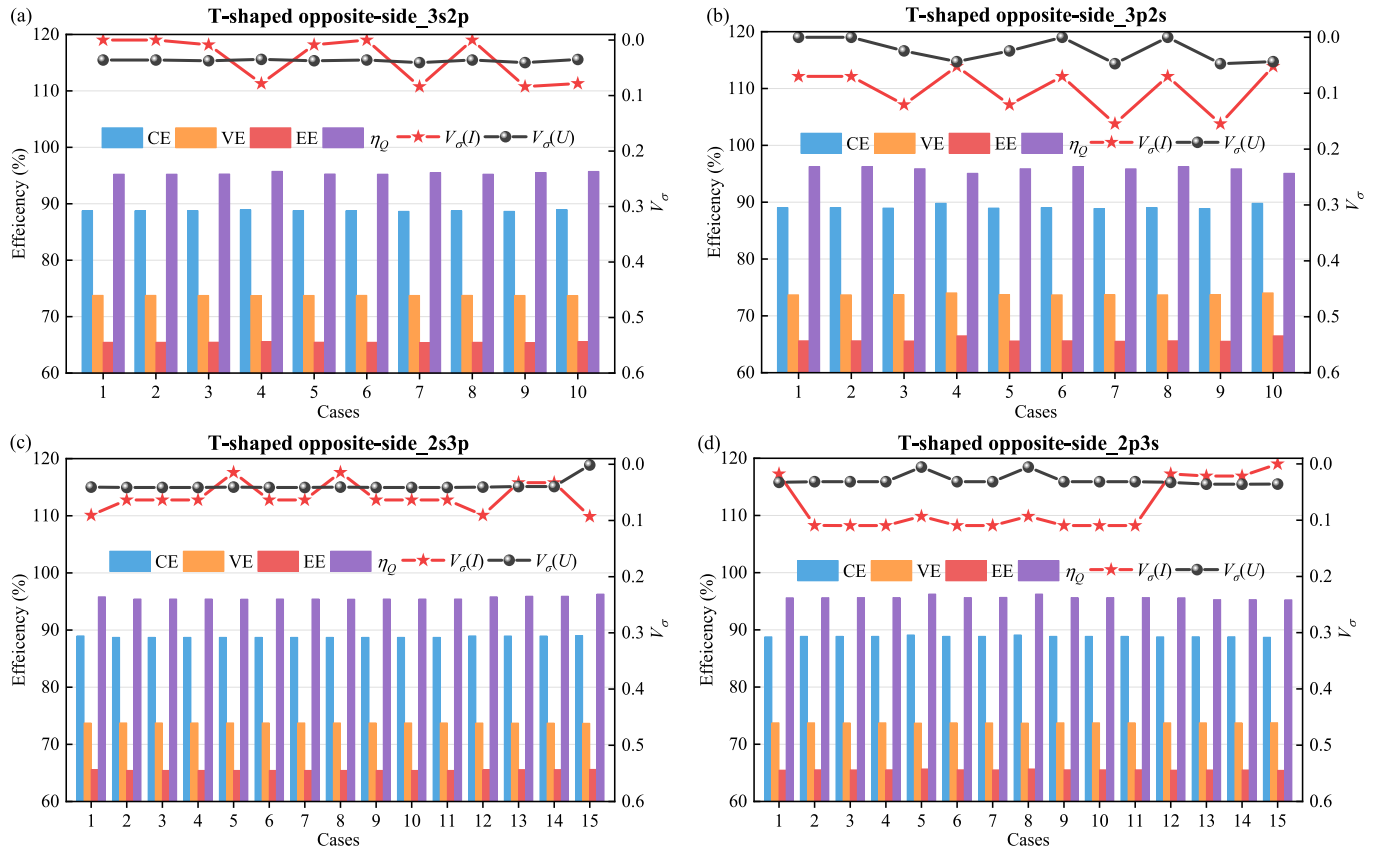


Fig. 10. Performance metrics of multi-stack VRB module under T-shaped opposite-side in different electrical mixed connections: (a) 3s2p; (b) 3p2s; (c) 2s3p; (d) 2p3s.

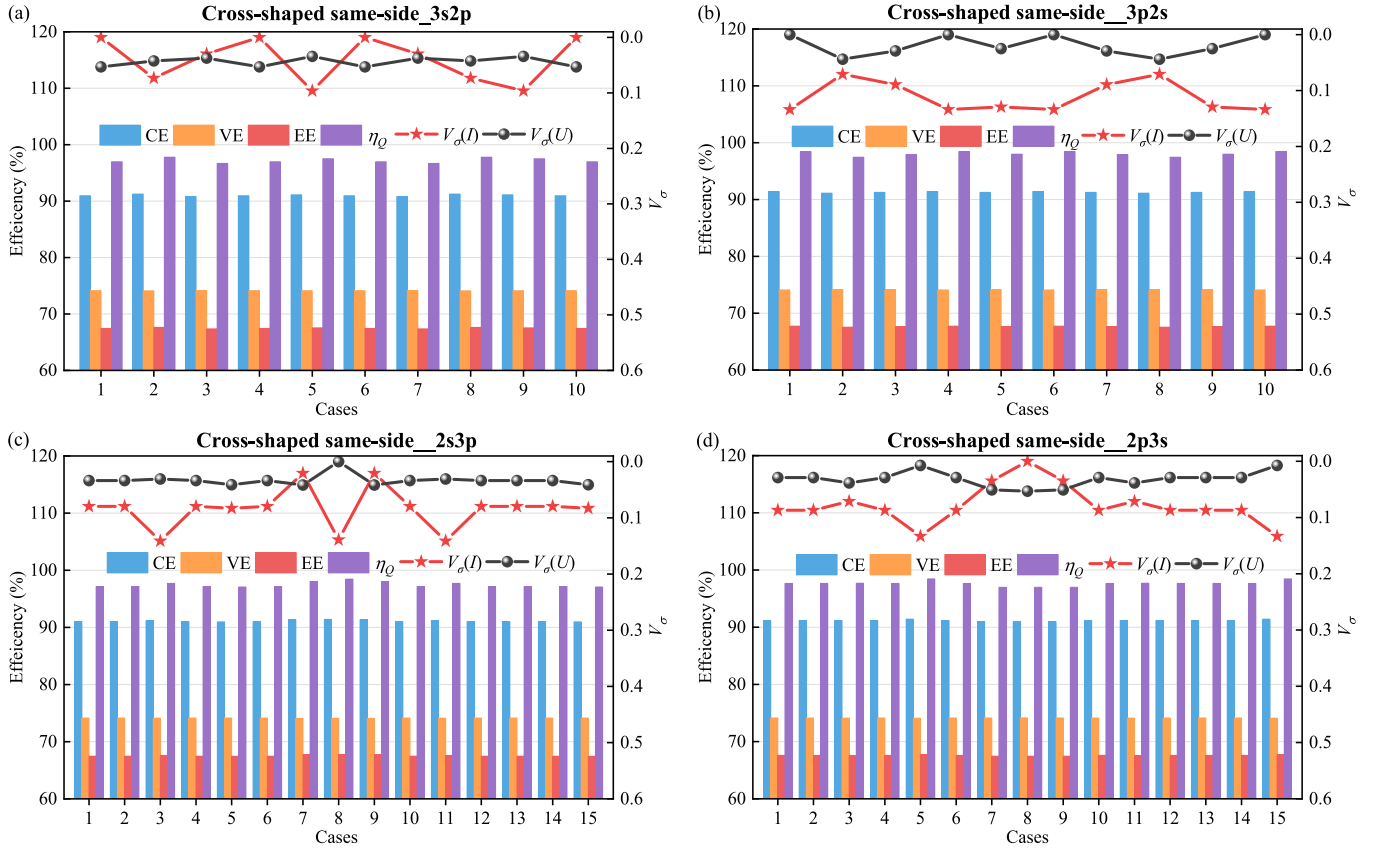


Fig. 11. Performance metrics of multi-stack VRB module under cross-shaped same-side in different electrical mixed connections: (a) 3s2p; (b) 3p2s; (c) 2s3p; (d) 2p3s.

suffers from significantly greater current inconsistency compared to other configurations. As a result, both configurations underperform compared to mixed connection configurations. In grid-scale energy storage applications, purely series or parallel multi-stack connections are generally not favored. Mixed configurations are preferred because they effectively mitigate the risk of system-wide failure from individual stack faults while better balancing voltage and current inconsistencies.

Table 7 presents the performance metrics for the T-shape same-side configuration. For the mixed connection, η_Q reaches its minimum when $V_{\sigma}(U)$ is at its highest in the 3s2p configuration. In contrast, η_Q reaches its maximum when $V_{\sigma}(U)$ is at its lowest in the 3p2s configuration. A similar pattern is observed for both series and parallel connections. This indicates a close relationship between voltage inconsistencies $V_{\sigma}(U)$ and the capacity utilization η_Q for a VRB multi-stack module, independent of the circuit connection type. η_Q is negatively correlated with the $V_{\sigma}(U)$. When a single stack reaches its cut-off voltage limit earlier than others, it prematurely terminates the charging/discharging process of the entire module, thereby limiting capacity utilization to that of the worst-performing stack. Consequently, a clear negative correlation is observed between η_Q and $V_{\sigma}(U)$ for all electrical connections. The same conclusion can be drawn from Tables 8–10. Specifically, as $V_{\sigma}(U)$ decreases, η_Q increases. This finding provides valuable insights for understanding and optimizing the performance of the multi-stack VRB module.

In summary, for practical applications, opposite-side or cross-shaped configurations are preferred when the design objective is to minimize $V_{\sigma}(U)$, which improves both OPS and η_Q and enhances the overall performance of the multi-stack VRB module.

4.6. Performance analysis under different temperature

In practice, ESSs have to face the challenges posed by temperature variations. In addition to normal temperature (25 °C), the section further analyses the performance of all configurations by discussing two extreme temperatures (0 °C and 35 °C).

In the analysis of pipe connections, the electrical connection remains the same, using the 6s as an example. Conversely, when examining the impact of electrical mixed connections, the pipe configuration is fixed as the cross-shaped opposite-side connection. Tables 11 and 12 present the performance of multi-stack VRB modules under different initial SOC for the 6 s electrical connection and the cross-shaped opposite-side pipe connection, respectively. To facilitate the analysis of the system performance under different electrical mixed connections, the optimal case under each electrical mixed connection is selected for comparison. Specifically, 3s2p and 3p2s are for Case 1 in their respective cases, and 2s3p and 2p3s are for Case 5 in their respective cases.

The decrease in CE at higher temperatures is mainly attributed to increased vanadium ion crossover. In contrast, low temperatures suppress ion diffusion and side reactions, leading to a slight increase of CE. VE, however, is affected by polarization losses. As temperature decreases, the electrolyte viscosity rises, which slows ion migration, increases internal resistance, and ultimately leads to a significant decrease in voltage efficiency. The opposite trend is observed at higher temperatures, where reduced resistance enhances VE.

The optimal temperature for VRBs typically falls between 20 and 30 °C. At high temperatures, the rapid drop in CE offsets the gain in VE, resulting in a net decrease in EE. At low temperatures, a significant decline in VE becomes the dominant factor, also leading to reduced EE. Nevertheless, since the model used in this study does not consider the temperature-dependent electrolyte viscosity, VE remains relatively

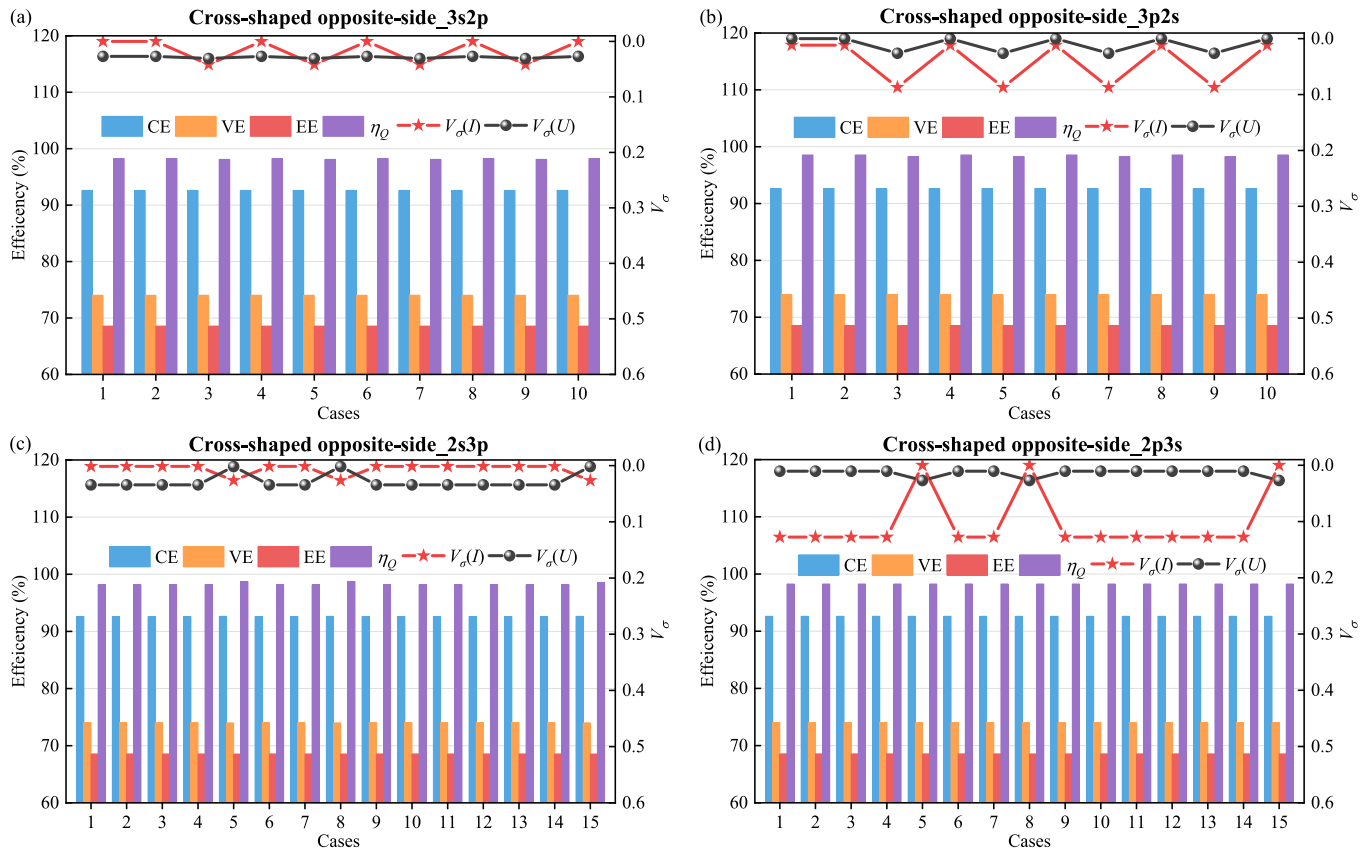


Fig. 12. Performance metrics of multi-stack VRB module under cross-shaped opposite-side design in different electrical mixed connections: (a) 3s2p; (b) 3p2s; (c) 2s3p; (d) 2p3s.

Table 6

Optimal OPS for different stack layouts under electrical mixed connections.

| Pipe connection | | OPS | | | | |
|-----------------|---------------|---------------------------|---------------------------|------------------|---------------------|---------|
| Pipe design | Feeding mode | 3s2p | 3p2s | 2s3p | 2p3s | Average |
| T-shaped | Same-side | Case 5: 1.5052 | Case 1: 1.4457 | Case 11: 1.4514 | Case 1: 1.4678 | 1.4675 |
| | Opposite-side | Case 1,2,6,8: 1.5710 | Case 1,2,6,8: 1.5489 | Case 5,8: 1.5532 | Case 15: 1.5532 | 1.5566 |
| Cross-shaped | Same-side | Case 1,4,6,10: 1.5052 | Case 3,7: 1.5371 | Case 7,9: 1.5949 | Case 8: 1.5910 | 1.5571 |
| | Opposite-side | Case 1,2,4,6,8,10: 1.6411 | Case 1,2,4,6,8,10: 1.6592 | Case 5,8: 1.6447 | Case 5,8,15: 1.6411 | 1.6465 |
| Average | | 1.5556 | 1.5477 | 1.5611 | 1.5633 | – |

Table 7

Performance metrics of multi-stack VRB module with T-shaped same-side connection.

| Metric | CE | VE | EE | η_Q | $V_{\sigma}(U)$ | $V_{\sigma}(I)$ |
|--------|--------|--------|--------|----------|-----------------|-----------------|
| 6s | 0.8513 | 0.7397 | 0.6297 | 0.9314 | 0.0494 | 0 |
| 6p | 0.8666 | 0.7386 | 0.6401 | 0.9679 | 0 | 0.2325 |
| 3s2p | 0.8538 | 0.7396 | 0.6315 | 0.9375 | 0.0471 | 0.0597 |
| 2s3p | 0.8419 | 0.7400 | 0.6230 | 0.9430 | 0.0418 | 0.1101 |
| 3p2s | 0.8543 | 0.7395 | 0.6318 | 0.9478 | 0.0284 | 0.1696 |
| 2p3s | 0.8521 | 0.7396 | 0.6302 | 0.9453 | 0.0413 | 0.1187 |

unchanged across different temperatures. As a result, EE at low temperatures is mainly influenced by the variation in CE. Consequently, both EE and OPS at 0 °C are higher than those at 25 °C.

Table 11 demonstrates that the cross-shaped opposite-side connection consistently yields a higher OPS than other pipe connections under all three temperatures. Table 12 indicates that the OPS of 3p2s is greater than the other electrical mixed connections at all temperatures. These results suggest that both the cross-shaped opposite-side pipe connection configuration and the 3p2s electrical mixed connection configuration

Table 8

Performance metrics of multi-stack VRB module with cross-shaped same-side connection.

| Metric | CE | VE | EE | η_Q | $V_{\sigma}(U)$ | $V_{\sigma}(I)$ |
|--------|--------|--------|--------|----------|-----------------|-----------------|
| 6s | 0.9096 | 0.7414 | 0.6744 | 0.9698 | 0.0532 | 0 |
| 6p | 0.9141 | 0.7409 | 0.6773 | 0.9845 | 0 | 0.1339 |
| 3s2p | 0.9102 | 0.7413 | 0.6747 | 0.9719 | 0.0441 | 0.0399 |
| 2s3p | 0.9108 | 0.7413 | 0.6752 | 0.9742 | 0.0331 | 0.0844 |
| 3p2s | 0.9129 | 0.7411 | 0.6766 | 0.9805 | 0.0100 | 0.1115 |
| 2p3s | 0.9117 | 0.7412 | 0.6758 | 0.9763 | 0.0320 | 0.0883 |

offer robust performance under varying temperature conditions. It makes them well-suited for practical applications where the ambient temperature fluctuates.

4.7. Performance analysis under different initial SOC

In practical applications, the impact of dynamic changes in SOC on system performance cannot be ignored. To better reflect the real-world conditions and validate the results, this section examines three initial

Table 9

Performance metrics of multi-stack VRB module with T-shaped opposite-side connection.

| Metric | CE | VE | EE | η_Q | $V_a(U)$ | $V_d(I)$ |
|--------|--------|--------|--------|----------|----------|----------|
| 6s | 0.8873 | 0.7377 | 0.6546 | 0.9525 | 0.0361 | 0 |
| 6p | 0.8904 | 0.7370 | 0.6562 | 0.9627 | 0 | 0.0700 |
| 3s2p | 0.8877 | 0.7376 | 0.6548 | 0.9541 | 0.0370 | 0.0342 |
| 2s3p | 0.8881 | 0.7375 | 0.6550 | 0.9561 | 0.0382 | 0.0584 |
| 3p2s | 0.8914 | 0.7378 | 0.6577 | 0.9588 | 0.0231 | 0.0934 |
| 2p3s | 0.8887 | 0.7374 | 0.6553 | 0.9565 | 0.0292 | 0.0761 |

Table 10

Performance metrics of multi-stack VRB module with cross-shaped opposite-side connection.

| Metric | CE | VE | EE | η_Q | $V_a(U)$ | $V_d(I)$ |
|--------|--------|--------|--------|----------|----------|----------|
| 6s | 0.9261 | 0.7403 | 0.6856 | 0.9825 | 0.027 | 0 |
| 6p | 0.9263 | 0.7400 | 0.6855 | 0.9854 | 0 | 0.0117 |
| 3s2p | 0.9261 | 0.7403 | 0.6856 | 0.9819 | 0.0285 | 0.0168 |
| 2s3p | 0.9261 | 0.7402 | 0.6855 | 0.9825 | 0.0277 | 0.0063 |
| 3p2s | 0.9262 | 0.7401 | 0.6855 | 0.9842 | 0.0105 | 0.0419 |
| 2p3s | 0.9261 | 0.7403 | 0.6856 | 0.9825 | 0.0139 | 0.1022 |

SOC levels: 20%, 50%, and 70%. Based on the OCV-SOC curve of the VRB, appropriate discharge cut-off voltages are applied to ensure the accuracy of efficiency calculations: 1.4 V for the 50% SOC and 1.4438 V for the 70% SOC.

Similar to the previous section, Tables 13 and 14 compare the performance of multi-stack VRB modules with 6s and cross-shaped opposite-side connections under different initial SOC, respectively. Longer charging/discharging duration amplify transport delay effects and result in more pronounced voltage inconsistencies. When one stack reaches the charging cut-off voltage, the charging process for the entire module stops, even though other stacks may not be fully charged, and their SOC levels are less than 1. During discharging, due to battery polarization, the

discharging duration is typically shorter than the charging duration, leading to a decrease in CE and, consequently, reduced EE. Moreover, the impact of transport delays during the discharging process is less significant than during charging. Therefore, the variance of the stack voltages at the discharging cut-off is smaller than that at the charging cut-off. As the discharging cut-off voltage increases with higher initial SOC, the discharging contribution in (16) decreases, leading to a reduction in η_Q and a corresponding drop in OPS.

Table 13 confirms that the cross-shaped opposite-side connection achieves higher OPS than the other pipe connections under three initial SOC levels. Furthermore, Table 14 shows that the OPS of 3p2s is greater than the other electrical mixed connections under three initial SOC levels. These results further validate that the cross-shaped opposite-side pipe connection configuration and the 3p2s electrical mixed connection configuration can be applied to real-world scenarios involving fluctuating SOC levels.

4.8. Analysis of cost-effectiveness

The 192-kW/1152-kWh ESS studied in the paper demonstrates economic viability based on the daily peak-to-valley electricity price difference. Fig. 13 illustrates typical electricity price fluctuations and the corresponding charging/discharging strategy adopted in certain areas. The off-peak electricity price is 0.2796 yuan/kWh (from 00:00 am to 8:00), during which the ESS charges for 6 h considering the potential operations such as maintenance and regular SOC equalization. The peak electricity price reaches 1.0548 yuan/kWh (from 10:00 to 12:00 and from 14:00 to 18:00), and the ESS discharges for a total of 6 h during these periods. The battery remains idle during other hours when the electricity price averages 0.7078 yuan/kWh. In summary, adopted operational strategy consists of one charging process and one discharging, e.g., one full cycle daily.

To evaluate the economic performance of the ESS, the levelized cost of storage (LCOS) is adopted. LCOS represents the average cost of storing and releasing one kWh of electricity per cycle over the full lifespan of the

Table 11

Comparison of performance metrics of multi-stack VRB module with 6s connection under different temperatures.

| Configuration condition | CE | VE | EE | η_Q | $V_a(U)$ | OPS |
|----------------------------------|----------------------------|--------|--------|----------|----------|--------|
| $T = 0\text{ }^{\circ}\text{C}$ | T-shaped Same-side | 0.8801 | 0.7392 | 0.6505 | 0.9460 | 1.5404 |
| | T-shaped Opposite-side | 0.9365 | 0.7407 | 0.6937 | 0.9844 | 1.6243 |
| | Cross-shaped Same-side | 0.9151 | 0.7374 | 0.6748 | 0.9651 | 1.6042 |
| | Cross-shaped Opposite-side | 0.9526 | 0.7397 | 0.7047 | 0.9953 | 1.6586 |
| $T = 25\text{ }^{\circ}\text{C}$ | T-shaped Same-side | 0.8513 | 0.7397 | 0.6297 | 0.9314 | 1.5117 |
| | T-shaped Opposite-side | 0.9096 | 0.7414 | 0.6744 | 0.9698 | 1.5910 |
| | Cross-shaped Same-side | 0.8871 | 0.7377 | 0.6544 | 0.9526 | 1.5711 |
| | Cross-shaped Opposite-side | 0.9259 | 0.7403 | 0.6854 | 0.9821 | 1.6419 |
| $T = 35\text{ }^{\circ}\text{C}$ | T-shaped Same-side | 0.8485 | 0.7396 | 0.6276 | 0.9258 | 1.5121 |
| | T-shaped Opposite-side | 0.9076 | 0.7413 | 0.6728 | 0.9641 | 1.5987 |
| | Cross-shaped Same-side | 0.8849 | 0.7374 | 0.6526 | 0.9479 | 1.5598 |
| | Cross-shaped Opposite-side | 0.9241 | 0.7402 | 0.6840 | 0.9773 | 1.6338 |

Table 12

Comparison of performance metrics of multi-stack VRB module with cross-shaped opposite-side connection under different temperatures.

| Configuration condition | CE | VE | EE | η_Q | $V_a(U)$ | $V_d(I)$ | OPS |
|----------------------------------|------|--------|--------|----------|----------|----------|--------|
| $T = 0\text{ }^{\circ}\text{C}$ | 3s2p | 0.9527 | 0.7397 | 0.7047 | 0.9951 | 0.0317 | 1.6682 |
| | 2s3p | 0.9529 | 0.7395 | 0.7046 | 0.9981 | 0.0004 | 1.6850 |
| | 3p2s | 0.9529 | 0.7395 | 0.7046 | 0.9981 | 0.0004 | 1.6895 |
| | 2p3s | 0.9527 | 0.7397 | 0.7047 | 0.9951 | 0.0317 | 1.6682 |
| $T = 25\text{ }^{\circ}\text{C}$ | 3s2p | 0.9261 | 0.7403 | 0.6856 | 0.9825 | 0.0270 | 1.6411 |
| | 2s3p | 0.9263 | 0.7400 | 0.6855 | 0.9854 | 0.0017 | 1.6427 |
| | 3p2s | 0.9263 | 0.7400 | 0.6855 | 0.9854 | 0.0026 | 1.6592 |
| | 2p3s | 0.9261 | 0.7403 | 0.6856 | 0.9825 | 0.0270 | 1.6411 |
| $T = 35\text{ }^{\circ}\text{C}$ | 3s2p | 0.9243 | 0.7401 | 0.6841 | 0.9772 | 0.0342 | 1.6271 |
| | 2s3p | 0.9245 | 0.7400 | 0.6841 | 0.9792 | 0.0026 | 1.6222 |
| | 3p2s | 0.9245 | 0.7400 | 0.6841 | 0.9792 | 0.0026 | 1.6298 |
| | 2p3s | 0.9243 | 0.7401 | 0.6841 | 0.9772 | 0.0342 | 1.6271 |

Table 13

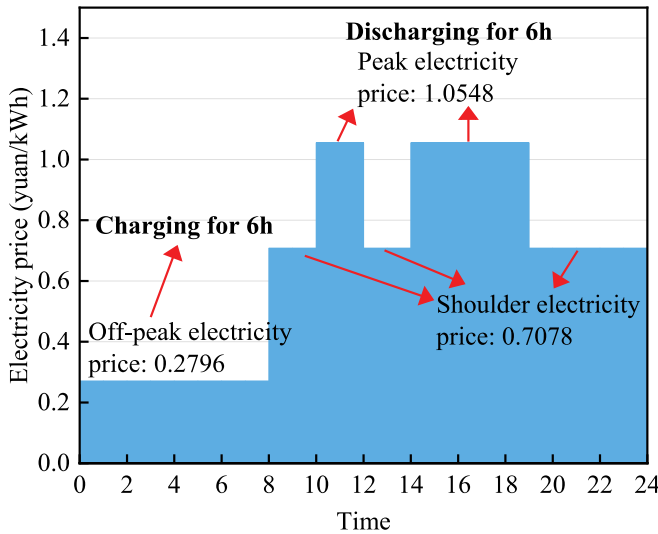
Comparison of performance metrics of multi-stack VRB module with 6s connection under initial different SOC.

| Configuration condition | | CE | VE | EE | η_Q | $V_a(U)$ | OPS |
|--|----------------------------|--------|--------|--------|----------|----------|---------------|
| SOC = 0.2 (Cut-off E_{OCV} : 1.329 V–1.671 V) | T-shaped Same-side | 0.8513 | 0.7397 | 0.6297 | 0.9314 | 0.0494 | 1.5117 |
| | T-shaped Opposite-side | 0.9096 | 0.7414 | 0.6744 | 0.9698 | 0.0532 | 1.5910 |
| | Cross-shaped Same-side | 0.8871 | 0.7377 | 0.6544 | 0.9526 | 0.0359 | 1.5711 |
| | Cross-shaped Opposite-side | 0.9259 | 0.7403 | 0.6854 | 0.9821 | 0.0256 | 1.6419 |
| SOC = 0.5 (Cut-off E_{OCV} : 1.4 V–1.671 V) | T-shaped Same-side | 0.7366 | 0.7439 | 0.5480 | 0.8932 | 0.0516 | 1.3895 |
| | T-shaped Opposite-side | 0.8471 | 0.7452 | 0.6313 | 0.9504 | 0.0387 | 1.5430 |
| | Cross-shaped Same-side | 0.8015 | 0.7416 | 0.5943 | 0.9256 | 0.0513 | 1.4686 |
| | Cross-shaped Opposite-side | 0.8764 | 0.7440 | 0.6520 | 0.9720 | 0.0362 | 1.5878 |
| SOC = 0.7 (cut-off for E_{OCV} : 1.4438 V–1.671 V) | T-shaped Same-side | 0.1612 | 0.7660 | 0.1234 | 0.7430 | 0.0513 | 0.8152 |
| | T-shaped Opposite-side | 0.7080 | 0.7474 | 0.5292 | 0.9168 | 0.0547 | 1.3912 |
| | Cross-shaped Same-side | 0.7183 | 0.7416 | 0.5327 | 0.8644 | 0.0477 | 1.3495 |
| | Cross-shaped Opposite-side | 0.7592 | 0.7453 | 0.5659 | 0.9535 | 0.0263 | 1.4930 |

Table 14

Comparison of performance metrics of multi-stack VRB module with cross-shaped opposite-side connection under initial different SOC.

| Configuration condition | | CE | VE | EE | η_Q | $V_a(U)$ | $V_a(I)$ | OPS |
|--|------|--------|--------|--------|----------|----------|----------|---------------|
| SOC = 0.2 (Cut-off E_{OCV} : 1.329 V–1.671 V) | 3s2p | 0.9261 | 0.7403 | 0.6856 | 0.9825 | 0.0270 | 0 | 1.6411 |
| | 2s3p | 0.9263 | 0.7400 | 0.6855 | 0.9854 | 0.0017 | 0.0265 | 1.6427 |
| | 3p2s | 0.9263 | 0.7400 | 0.6855 | 0.9854 | 0.0026 | 0.0091 | 1.6592 |
| | 2p3s | 0.9261 | 0.7403 | 0.6856 | 0.9825 | 0.0270 | 0 | 1.6411 |
| SOC = 0.5 (Cut-off E_{OCV} : 1.4 V–1.671 V) | 3s2p | 0.8768 | 0.7437 | 0.6521 | 0.9726 | 0.0468 | 0 | 1.5779 |
| | 2s3p | 0.8909 | 0.7476 | 0.6660 | 0.9702 | 0.0427 | 0.0503 | 1.5432 |
| | 3p2s | 0.8909 | 0.7476 | 0.6660 | 0.9702 | 0.0427 | 0.0353 | 1.5582 |
| | 2p3s | 0.8768 | 0.7437 | 0.6521 | 0.9726 | 0.0468 | 0 | 1.5779 |
| SOC = 0.7 (Cut-off E_{OCV} : 1.4438 V–1.671 V) | 3s2p | 0.7583 | 0.7453 | 0.5652 | 0.9529 | 0.0271 | 0 | 1.4910 |
| | 2s3p | 0.7603 | 0.7447 | 0.5662 | 0.9596 | 0.0020 | 0.0141 | 1.5097 |
| | 3p2s | 0.7603 | 0.7447 | 0.5662 | 0.9596 | 0.0020 | 0.0056 | 1.5182 |
| | 2p3s | 0.7583 | 0.7453 | 0.5652 | 0.9529 | 0.0271 | 0 | 1.4910 |

**Fig. 13.** Daily electricity price variation and ESS operational strategies.

ESS, and is calculated by [32]:

$$LCOS = \frac{LOSS_{power} + Cost_{O\&M} + Cost_{install}}{Cycle_{life}} \quad (20)$$

where $LOSS_{power}$ denotes the power loss cost, $Cost_{O\&M}$ is the operation and maintenance costs, $Cost_{install}$ considers the installation cost, and $Cycle_{life}$ represents the total equivalent full cycles over the system lifespan. Each term is defined as follows:

$$LOSS_{power} = P_p \left(\frac{1}{\eta_{CE}} - 1 \right) \sum_{y=1}^Y \frac{N_{cycle}(y)}{(1 + DR)^y} \quad (21)$$

$$Cost_{O\&M} = \sum_{y=1}^Y \frac{O\&M(y)}{(1 + DR)^y} \quad (22)$$

$$Cost_{install} = \left(\frac{C_E}{EE} + \frac{C_p}{d_{dch}} \right) \quad (23)$$

$$Cycle_{life} = \sum_{y=1}^Y \frac{N_{cycle}(y)}{(1 + DR)^y} \quad (24)$$

where p_p is the electricity purchase price, η_{CE} is the cycle efficiency of the ESS, $N_{cycle}(y)$ is the number of equivalent 100% cycles in y th year, DR is the discount rate, C_E and C_p denote the energy and power installation costs, respectively, d_{dch} is the rated discharge duration, Y represent the system lifespan in years, and $O\&M(y)$ is the operation and maintenance cost ratio in the y th year.

Table 15

Economic parameters of a 192-kW/1152-kWh energy storage system.

| Symbol | Meaning | Value |
|------------------|---|---------------|
| LCOS | Levelized cost of storage | – |
| $LOSS_{power}$ | Power loss | – |
| $Cost_{O\&M}$ | Operational and maintenance cost | – |
| $Cost_{install}$ | Installation cost | – |
| $Cycle_{life}$ | Cycle number of the full life of the system | – |
| P_p | Electricity purchase price | 0.2706 yuan |
| η_{CE} | cycle efficiency of the ESS | 82% |
| Y | System lifespan | 30 years |
| $N_{cycle}(y)$ | Equivalent 100% cycle number of y th year | $350/\eta_Q$ |
| DR | Discount rate | 7% |
| $O\&M(y)$ | Operation and maintenance cost ratio of the y th year | 5% |
| C_E | Energy installation cost | 1500 yuan/kWh |
| C_p | Power installation cost | 6000 yuan/kW |
| d_{dch} | Discharge duration | 6 h |

The economic parameters for the 192-kW/1152-kWh ESS are listed in Table 15. The baseline number of cycles per year is set to 350, considering the annual maintenance of the ESS. In practical operations, however, the actual value is set to $350\eta_Q$ due to the varying capacity utilization efficiencies of different configurations. Operational and maintenance costs are assumed to be 5% of the total capital cost annually. Since the output power and storage capacity of a VRB ESS can be configured independently, installation costs are divided into C_E and C_P . The price of electrolyte raw materials V_2O_5 is 100,000 yuan/ton, resulting in an energy installation cost of approximately 1500 yuan/kWh. The power installation price of the ESS is assumed to be 6000 yuan/kW for durations of 1 h., excluding the cost of electrolyte storage systems.

Fig. 14(a) shows the LCOS values for four pipe connections under the 6s configuration. A lower LCOS indicates better economic performance. The cross-shaped opposite-side configuration exhibits the lowest LCOS of 1.274, at least 0.026 lower than the other three pipe connections, indicating superior cost-effectiveness in pipe connection design.

Fig. 14(b) presents the LCOS for various electrical mixed connections under the cross-shaped, opposite-side configuration. The 3p2s configuration demonstrates the lowest LCOS at 1.268, which outperforms all other electrical configurations by at least 0.002. This confirms that 3p2s is the most cost-effective electrical mixed connection.

4.9. Feasibility analysis of optimal configurations for large-scale applications

Table 16 presents a comprehensive feasibility analysis of the optimal configurations for large-scale VRB systems from different perspectives. In large-scale applications, multi-stack modules are typically connected in series, parallel, and mixed configurations, resulting in uneven load distribution among stack, leading to differences in efficiency and a decline in overall system performance. Optimal configuration design can mitigate these inconsistencies and significantly enhance system performance.

One of the key limitations of multi-stack VRB modules is their relatively low level of integration and large physical footprint, which restricts their deployment in space. However, the adoption of an optimal pipe connection can effectively enhance multi-stack module integration and reduce spatial requirements.

Multi-stack systems are also vulnerable to faults in single stacks. A failure in a single stack can compromise the overall system, particularly in pure series configurations. Furthermore, variations in stack lifespan and cycling performance introduce long-term stability challenges. The use of optimal electrical mixed connections has 3p2s can effectively mitigate these issues by isolating the impact of single-stack failures and distributing electrical loads more evenly.

Another critical consideration is the high initial capital and

maintenance cost associated with large numbers of battery cells, integrated circuits, and control components. To address this, the comparative analysis of LCOS is conducted to identify the most economically viable configuration. The results demonstrate that the combination of cross-shaped opposite-side pipe layout and 3p2s electrical connection yields the lowest LCOS and, therefore, the best cost-effectiveness.

When deploying large-scale energy storage systems, it is also necessary to consider how to expand the number of electrical stacks without significantly affecting performance. The optimal configuration is obtained based on both piping connections and electrical connections, respectively. Uneven electrolyte flow can lead to efficiency differences between stacks and thermal imbalance problems. High-precision equipment is required for electrolyte flow control and monitoring. Otherwise, charging and discharging efficiency degradation or stack damage. The electrolyte transport delay model developed in the paper provides a mechanistic solution to capture and mitigate these effects reliably.

In summary, although multi-stack VRB modules offer technical feasibility for large-scale applications, they also face a set of engineering and economic challenges. These can be effectively addressed through the strategic implementation of optimal piping and electrical connections, enabling the broader deployment of VRB technology in grid-scale ESSs.

5. Conclusions

This study investigates the performance of a multi-stack VRB module using a six-stack system as a case study. A comprehensive classification of pipe and electrical connections is provided, with four types of pipe connections (T-shape same-side, T-shape opposite-side, cross-shaped same-side, and cross-shaped opposite-side) and 52 electrical configurations (3s2p, 3p2s, 2s3p, 2p3s). The simulation results based on all 208 multi-stack connections reveal that the cross-shaped opposite-side configuration provides the most favorable performance, highlighting the advantages of a compact pipe arrangement with an opposite-side tank design. Additionally, among the mixed electrical connections, the 3p2s configuration demonstrates the highest key performance indicator, suggesting an optimal balance between voltage and current distribution. Beyond these findings, the study also highlights the critical role of minimizing voltage inconsistency $V_e(U)$ and maximizing current consistency $V_e(I)$ in enhancing capacity utilization η_Q and overall efficiency. The study further explores the impact of different initial states of charge and operating temperatures. In addition, an in-depth techno-economic assessment is performed to evaluate the practical feasibility of all considered configurations. These insights provide a systematic framework for optimizing the design and operation of multi-stack VRB ESSs, which contributes to improved charging-discharging efficiency and

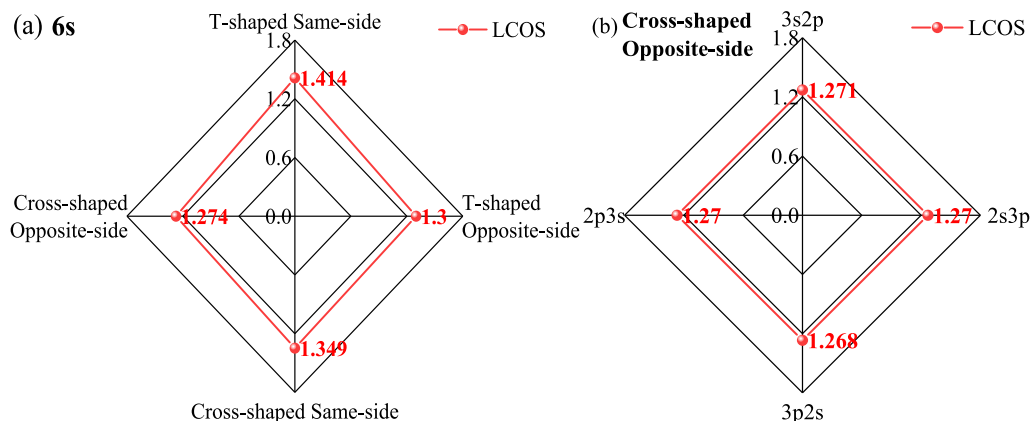


Fig. 14. LCOS comparisons for different configurations: (a) 6 s; (b) Cross-shaped opposite-side.

Table 16
Feasibility analysis of optimal configurations for large-scale applications.

| Practical feasibility | Technical implementation challenge | Potential obstacle | Possible solution |
|-----------------------|---|---|---|
| Configuration | Uneven load distribution | Poor system performance | Optimal configuration to improve system performance |
| Integration | Large volume | Unsatisfactory requirements in limited space | Optimal pipe connection to improve integration |
| Safety and stability | Overall failure due to failure of single stack | Low system stability | Optimal electrical connection to enhance the stability |
| Cost-effectiveness | Various battery cells, integrated circuits, and control systems | Higher initial investment and maintenance costs | Economical configuration based on LCOS |
| Scalability | Considering system scalability for large-scale deployments | Capacity mismatch | Optimal pipe and electrical connections based on η_Q |
| Electrolyte control | Uneven flow of electrolyte | Low multi-stack efficiency | Modeling transport delays |

capacity utilization, reliability, and system scalability in large-scale energy applications. The methodology used in the paper can also be applied to other types of flow battery systems and similar energy storage technologies.

Future research should explore experimental validation of these configurations and investigate advanced control strategies to further enhance system performance under dynamic operating conditions.

CRediT authorship contribution statement

Shaojin Wang: Investigation, Methodology, Writing - original draft. **Yang Li:** Supervision, Writing - reviewing & editing. **Chengyan Li:** Conceptualization, Writing- Reviewing & Editing. **Xifeng Lin:** Data analysis, Writing- Reviewing & Editing. **Wenbo Ma:** Methodology. **Nannan Tong:** Software. **Binyu Xiong:** Investigation, supervision, Writing- Reviewing & Editing.

Declaration of competing interest

The authors declare that they have no known competing financial interests or personal relationships that could have appeared to influence the work reported in this paper.

Acknowledgements

This work is supported by the National Natural Science Foundation of China (No. 52177221).

Data availability

Data will be made available on request.

References

- [1] Q. Wang, Z. Zhang, P. Lv, Z. Peng, J. Yang, Poly(terphenyl pyridine) based amphoteric and anion exchange membranes with high ionic selectivity for vanadium redox flow batteries, *Chem. Eng. J.* 505 (2025) 158922, <https://doi.org/10.1016/j.cej.2024.158922>.
- [2] L.F. Pilonetto, F. Staciaki, E. Nóbrega, E.B. Carneiro-Neto, J. da Silva, E. Pereira, Mitigating the capacity loss by crossover transport in vanadium redox flow battery: a chemometric efficient strategy proposed using finite element method simulation, *Chem. Eng. J.* 474 (2023) 145336, <https://doi.org/10.1016/j.cej.2023.145336>.
- [3] Z. Huang, A. Mu, L. Wu, B. Yang, Y. Qian, J. Wang, Comprehensive analysis of critical issues in all-vanadium redox flow battery, *ACS Sustain. Chem. Eng.* 10 (2022) 7786–7810, <https://doi.org/10.1021/acssuschemeng.2c01372>.
- [4] T. Ouyang, M. Zhang, P. Qin, X. Tan, Flow battery energy storage system for microgrid peak shaving based on predictive control algorithm, *Appl. Energy* 356 (2024) 122448, <https://doi.org/10.1016/j.apenergy.2023.122448>.
- [5] J. Paick, J.S. Yi, D. Lee, Detection and analysis of inner potential dynamics in vanadium redox flow batteries, *Chem. Eng. J.* 481 (2024) 148543, <https://doi.org/10.1016/j.cej.2024.148543>.
- [6] M. Khatibi, S.N. Ashrafizadeh, Ion transport in intelligent nanochannels: a comparative analysis of the role of electric field, *Anal. Chem.* 95 (2023) 18188–18198, <https://doi.org/10.1021/acs.analchem.3c03809>.
- [7] X. Shi, O.C. Esan, X. Huo, Y. Ma, Z. Pan, L. An, et al., Polymer electrolyte membranes for vanadium redox flow batteries: fundamentals and applications, *Prog. Energy Combust. Sci.* 85 (2021) 100926, <https://doi.org/10.1016/j.pecs.2021.100926>.
- [8] S.N. Oreiro, A. Bentien, J. Sloth, M. Rahimi, M.B. Madsen, T. Drechsler, Crossover analysis in a commercial 6 kW/43kAh vanadium redox flow battery utilizing anion exchange membrane, *Chem. Eng. J.* 490 (2024) 151947, <https://doi.org/10.1016/j.cej.2024.151947>.
- [9] E. Hampson, J.C. Duburg, J. Casella, T.J. Schmidt, L. Gubler, A simple approach to balancing conductivity and capacity fade in vanadium redox flow batteries by the tunable pretreatment of polybenzimidazole membranes, *Chem. Eng. J.* 485 (2024) 149930, <https://doi.org/10.1016/j.cej.2024.149930>.
- [10] M. Jafari, A. Sakti, A. Botterud, Optimization of electrolyte rebalancing in vanadium redox flow batteries, *IEEE Trans. Energy Convers.* 37 (2022) 748–751, <https://doi.org/10.1109/TEC.2021.3136769>.
- [11] L. Barelli, M. Longo, P.A. Ottaviano, D. Pelosi, D. Zaninelli, F. Gallorini, Vanadium redox flow battery integration in on-board electric systems for hybrid marine applications, *IEEE Trans. Ind. Appl.* 60 (2024) 6539–6546, <https://doi.org/10.1109/TIA.2024.3397786>.
- [12] A.M. Demeku, C.-H. Guo, D.M. Kabtamu, Z.-J. Huang, G.-C. Chen, A.W. Bayeh, et al., Enhanced electrochemical performance of copper-doped cobalt oxide nanowire-modified graphite felt as positive electrode material for vanadium redox flow batteries, *Chem. Eng. J.* 505 (2025) 159170, <https://doi.org/10.1016/j.cej.2024.159170>.
- [13] H. Chen, M. Cheng, X. Feng, Y. Chen, F. Chen, J. Xu, Analysis and optimization for multi-stack vanadium flow battery module incorporating electrode permeability, *J. Power Sources* 515 (2021) 230606, <https://doi.org/10.1016/j.jpowsour.2021.230606>.
- [14] F. Chen, H. Gao, H. Chen, C. Yan, Evaluation of thermal behaviors for the multi-stack vanadium flow battery module, *J. Energy Storage* 27 (2020) 101081, <https://doi.org/10.1016/j.est.2019.101081>.
- [15] H.-W. Chou, F.-Z. Chang, H.-J. Wei, B. Singh, A. Arpornwichanop, P. Jienkulsawad, et al., Locating shunt currents in a multistack system of all-vanadium redox flow batteries, *ACS Sustain. Chem. Eng.* 9 (2021) 4648–4659, <https://doi.org/10.1021/acssuschemeng.1c00287>.
- [16] A. Trovo, G. Marini, A. Sutto, P. Motto, M. Giomo, F. Moro, et al., Standby thermal model of a vanadium redox flow battery stack with crossover and shunt-current effects, *Appl. Energy* 240 (2019) 893–906, <https://doi.org/10.1016/j.apenergy.2019.02.067>.
- [17] Q. Ye, J. Hu, P. Cheng, Z. Ma, Design trade-offs among shunt current, pumping loss and compactness in the piping system of a multi-stack vanadium flow battery, *J. Power Sources* 296 (2015) 352–364, <https://doi.org/10.1016/j.jpowsour.2015.06.138>.
- [18] F.T. Wandschneider, S. Roehm, P. Fischer, K. Pinkwart, J. Tuebke, H. Nirschl, A multi-stack simulation of shunt currents in vanadium redox flow batteries, *J. Power Sources* 261 (2014) 64–74, <https://doi.org/10.1016/j.jpowsour.2014.03.054>.
- [19] X. Zhao, Y.-B. Kim, S. Jung, Shunt current analysis of vanadium redox flow battery system with multi-stack connections, *J. Energy Storage* 73 (2023) 109233, <https://doi.org/10.1016/j.est.2023.109233>.
- [20] J. Tian, Y. Fan, T. Pan, X. Zhang, J. Yin, Q. Zhang, A critical review on inconsistency mechanism, evaluation methods and improvement measures for lithium-ion battery energy storage systems, *Renew. Sustain. Energy Rev.* 189 (2024) 113978, <https://doi.org/10.1016/j.rser.2023.113978>.
- [21] Z. Chen, W. Liu, T. Xia, E. Pan, Consistency evaluation for lithium-ion battery energy storage systems based on approximate low-rank representation and hypersphere concentration, *IEEE Trans Ind Electron* (2024), <https://doi.org/10.1109/TIE.2024.3463029>.
- [22] J. Tian, G. Chang, X. Liu, Z. Wei, H. Wen, L. Yang, et al., Consistency evaluation of electric vehicle battery pack: multi-feature information fusion approach, *IEEE Trans Veh Technol* 72 (2023) 14103–14114, <https://doi.org/10.1109/TVT.2023.3284058>.
- [23] H. Xu, S. Yang, B. Li, Pressure effects and countermeasures in solid-state batteries: a comprehensive review, *Adv. Energy Mater.* (2024) 14, <https://doi.org/10.1002/aenm.202303539>.
- [24] X. Liu, G. Chang, J. Tian, Z. Wei, X. Zhang, P. Wang, Flexible path planning-based reconfiguration strategy for maximum capacity utilization of battery pack, *J. Energy Chem.* 86 (2023) 362–372, <https://doi.org/10.1016/j.jechem.2023.07.040>.

- [25] H. Chen, X. Li, H. Gao, J. Liu, C. Yan, A. Tang, Numerical modelling and in-depth analysis of multi-stack vanadium flow battery module incorporating transport delay, *Appl. Energy* 247 (2019) 13–23, <https://doi.org/10.1016/j.apenergy.2019.04.034>.
- [26] H. Chen, S. Wang, H. Gao, X. Feng, C. Yan, A. Tang, Analysis and optimization of module layout for multi-stack vanadium flow battery module, *J. Power Sources* 427 (2019) 154–164, <https://doi.org/10.1016/j.jpowsour.2019.04.054>.
- [27] M. Khatibi, A. Mojavezi, E. Pourjafarabadi, Harvesting blue energy: pH-regulated nanochannels inspired by carbon nanostructures, *Phys. Fluids* 35 (2023) 102017, <https://doi.org/10.1063/5.0170927>.
- [28] B. Xiong, J. Tang, Y. Li, C. Xie, Z. Wang, X. Zhang, et al., Design of a two-stage control strategy of vanadium redox flow battery energy storage systems for grid application, *IEEE Trans. Sustain. Energy* 13 (2022) 2079–2091, <https://doi.org/10.1109/TSTE.2022.3181751>.
- [29] W.-J. Zou, Y.-B. Kim, S. Jung, Capacity fade prediction for vanadium redox flow batteries during long-term operations, *Appl. Energy* 356 (2024) 122329, <https://doi.org/10.1016/j.apenergy.2023.122329>.
- [30] R. Xiong, B. Xiong, Q. Zhang, S. Shi, Y. Su, D. Zhang, Capacity fading model of vanadium redox flow battery considering water molecules migration, *Int. J. Green Energy* 19 (2022) 1613–1622, <https://doi.org/10.1080/15435075.2021.2015599>.
- [31] A. Tang, J. Bao, M. Skyllas-Kazacos, Studies on pressure losses and flow rate optimization in vanadium redox flow battery, *J. Power Sources* 248 (2014) 154–162, <https://doi.org/10.1016/j.jpowsour.2013.09.071>.
- [32] C. Buchanan, N. Singh, Levelized cost of electricity and greenhouse gas emissions of Ce- and V-based redox flow batteries, *J. Power Sources* 582 (2023) 233535, <https://doi.org/10.1016/j.jpowsour.2023.233535>.